AIAA JOURNAL
Vol. 46, No. 6, June 2008

Enhancing the Robustness of Aeroelastic Instability Suppression Using Multi-Degree-of-Freedom Nonlinear Energy Sinks

Young S. Lee,* Alexander F. Vakakis,† Lawrence A. Bergman,‡ D. Michael McFarland,§ and Gaëtan Kerschen¶
University of Illinois at Urbana–Champaign, Urbana, Illinois 61801

DOI: 10.2514/1.30302

In this last of a three paper sequence, we use simultaneous multimodal broadband targeted energy transfers to multi-degree-of-freedom nonlinear energy sinks to improve the robustness of aeroelastic instability suppression of a rigid wing with structural nonlinearities. A numerical bifurcation analysis of limit cycle oscillations of the wing with the multi-degree-of-freedom nonlinear energy sinks attached shows that controlling the lower parameter value for limit point cycle bifurcation to occur above Hopf bifurcation is crucial to enhancing the robustness of limit cycle oscillation suppression. We demonstrate that multi-degree-of-freedom nonlinear energy sinks can greatly enhance the robustness of limit cycle oscillation suppression, compared with single-degree-of-freedom nonlinear energy sinks (which were studied in our previous papers), with a much smaller total mass. We also investigate the nonlinear modal interactions that occur between the aeroelastic modes and the multi-degree-of-freedom nonlinear energy sinks, in an effort to gain a physical understanding of the mechanisms governing instability suppression. We demonstrate that a properly designed multi-degree-of-freedom nonlinear energy sink provides robustness of aeroelastic instability suppression by efficiently, passively, and rapidly transferring a significant portion of unwanted vibration energy to the furthest mass of the nonlinear energy sink. Consideration of other types of multi-degree-of-freedom nonlinear energy sinks suggests that the robustness enhancement is achieved by the concentrated mass effect of the attached nonlinear energy sinks.

Nomenclature

b	=	semichord length, $c/2$, where c is a chord length
C; C_1	=	nondimensional coefficients for essentially nonlinear coupling stiffness, $b^2k_s/m\omega_\alpha^2$; linear coupling stiffness, $k/m\omega_\alpha^2$
$C_{L,\alpha}$	=	lift curve slope, $\partial C_L/\partial\alpha\|_{\alpha=0}$ where C_L is the lift coefficient
c_1, c_2	=	nonlinear heave and pitch stiffness factors
d, δ	=	offset attachment of the nonlinear energy sink to the wing, measured from and positive ahead of the elastic axis; nondimensional offset, d/b
E_d^{NES}	=	instantaneous energy dissipation by a nonlinear energy sink
E^{input}	=	instantaneous input energy given to the aeroelastic system
E^{total}	=	instantaneous total energy of the aeroelastic system coupled with a nonlinear energy sink
$E^{y,\alpha,v}$	=	instantaneous modal energies in heave, pitch, and nonlinear energy sink modes, respectively
e; γ	=	location of the aerodynamic center measured from the elastic axis (positive ahead of elastic axis); nondimensional parameter, e/b
h, α, z	=	heave (positive downward), pitch (positive clockwise), and nonlinear energy sink (positive downward) degrees of freedom
K_h, K_α	=	coefficients of linear heave and pitch stiffnesses
k	=	coefficient of linear coupling stiffness
L, M	=	lift and aerodynamic moment acting at the aerodynamic center, respectively; the equivalent aerodynamic forces at the elastic axis are $L_{\mathrm{ea}} = L$ and $M_{\mathrm{ea}} = M + eL \approx eL$ for small angles
m, I_α	=	mass of the airfoil and its mass moment of inertia with respect to the elastic axis
m_s, k_s, c_s	=	mass, essentially nonlinear stiffness coefficient, and damping in the nonlinear energy sink
q	=	dynamic pressure, $\frac{1}{2}\rho_\infty U^2$, where ρ_∞ is the density of the flow
r_α	=	radius of gyration of the cross section of the wing, $\sqrt{I_\alpha/(mb^2)}$
S	=	planform area of the wing
S_α; x_α	=	mass unbalance in the airfoil, mx_{cg}; its nondimensional parameter, S_α/mb, or x_{cg}/b
$\bar{T}$, $\bar{V}$	=	instantaneous kinetic and potential energies of the aeroelastic system coupled with a nonlinear energy sink
t, τ	=	physical and nondimensional times ($\tau = \omega_\alpha t$)
U	=	constant and uniform flow speed around the wing
$W_{\mathrm{nc}}^{y,\alpha}$	=	instantaneous nonconservative work done by heave and pitch modes, respectively
x_{cg}	=	location of the center of gravity measured from the elastic axis (positive aft of the elastic axis)
y, v	=	nondimensional heave ($y = h/b$) and nonlinear energy sink ($v = z/b$) modes
ϵ	=	mass ratio between the nonlinear energy sink and the wing, m_s/m
Θ	=	reduced speed of the flow, $U/b\omega_\alpha$

Received 6 February 2007; accepted for publication 4 January 2008.

*Postdoctoral Research Associate, Department of Aerospace Engineering, 104 South Wright Street.
†Adjunct Professor, Departments of Mechanical Science and Engineering, and Aerospace Engineering; also Professor, School of Applied Mathematical and Physical Sciences, National Technical University of Athens, Athens, Greece.
‡Professor, Department of Aerospace Engineering, 104 South Wright Street. Associate Fellow AIAA.
§Research Associate Professor, Department of Aerospace Engineering, 104 South Wright Street. Senior Member AIAA.
¶Assistant Professor, Aerospace and Mechanical Engineering Department, Université de Liège, Liège, Belgium.

λ = nondimensional linear viscous damping in the nonlinear energy sink, $c_s/(m_s\omega_\alpha)$
μ = density ratio, $\rho_\infty bS/2m$
ξ_y, ξ_α = nondimensional nonlinear heave and pitch stiffness factors ($\xi_y = c_1 b^2\Omega^2$, $\xi_\alpha = c_2 r_\alpha^2$)
Ω = frequency ratio, ω_h/ω_α where $\omega_h = \sqrt{K_h/m}$ and $\omega_\alpha = \sqrt{K_\alpha/I_\alpha}$

Subscripts

ac = aerodynamic center
cg = center of gravity
d = dissipation
ea = elastic axis
F = flutter
H = Hopf bifurcation
nc = nonconservative
RE = robustness enhancement

Superscripts

$\dot{}$ = $\mathrm{d}/\mathrm{d}t$
$'$ = $\mathrm{d}/\mathrm{d}\tau$

I. Introduction

THREE distinct mechanisms for suppressing aeroelastic instabilities (referred to henceforth as "instabilities") by applying a single-degree-of-freedom nonlinear energy sink (SDOF NES) to a rigid wing (Fig. 1) were studied theoretically and experimentally in Lee et al. [1,2] These mechanisms were characterized by recurrent burstouts and suppressions, partial, and complete suppression of the aeroelastic instabilities, respectively. Furthermore, nonlinear modal interactions between the aeroelastic and NES modes were investigated in these papers.

It was shown that a series of resonance captures was the underlying dynamic mechanism for the efficient suppression of instabilities. These results were numerically verified by examining the instantaneous frequencies and the corresponding transitions on newly defined frequency-energy plots, as well as by analyzing the nonlinear time series of the responses by means of empirical mode decomposition combined with the Hilbert transform. Use of two-frequency averaging after complexification of the system variables provided analytical verification of all the underlying mechanisms of instability suppression.

An investigation of instantaneous nonlinear modal interactions supported the idea of vigorous energy exchanges between modes of the wing and the NES during the occurrence of resonance captures. In particular, a comparison of the amount of input energy that comes from the nonconservative work of the flow and the energy dissipation by the NES provided a clear picture of what happens during different suppression mechanisms. Complete elimination of aeroelastic instabilities turned out to hinge on the successful creation of efficient irreversible energy flows from the aeroelastic system to the NES, that is, rapid energy transfer to and energy dissipation by the NES.

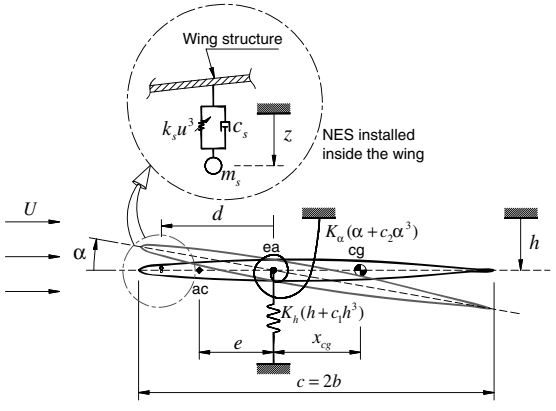

Fig. 1 2-DOF rigid wing model coupled with an SDOF NES.

A bifurcation analysis of the dynamics with respect to the offset (δ) and the reduced velocity (Θ) revealed that those suppression mechanisms are closely related to the bifurcation behavior of the limit cycle oscillations (LCOs) of the combined wing–NES system. That is, the recurring burstouts and suppressions of aeroelastic instabilities, which result in nonlinear beating responses, are associated with Neimark–Sacker (NS) bifurcations of periodic motions. Complete LCO elimination is due to the delayed occurrence of the Hopf bifurcation of a trivial equilibrium position. Finally, the generation of a periodic motion leads to an LCO with partially attenuated amplitude compared with the LCO of the wing with no NES attached.

Understanding the LCO branches formed through NS and, particularly, limit point cycle (LPC) bifurcations plays a key role in interpreting the robustness of each suppression mechanism. For example, if one of the two LPC bifurcation points occurs lower than a Hopf bifurcation point, then the LCO branch, which is generated after a delayed Hopf bifurcation and possesses lower amplitudes than the original LCO response, may be nonrobust or vulnerable to disturbances; it will exhibit a branch transition (or jump). In this regard, NES attachments with negative offsets generally provide better LCO suppression; that is, the lower LPC bifurcation point is usually generated above the Hopf bifurcation with NES negative offsets.

At this point, one can raise the issue of enhancing robustness for instability suppression through broadband, passive targeted energy transfers (TETs). To address this, we consider multi-degree-of-freedom (MDOF) NES configurations. The MDOF NES can be coupled either in series or in parallel to the primary system. However, it will be shown that the MDOF NES coupled in series will exhibit better enhancement due to the effect of mass concentration (this will be discussed in Secs. III and IV).

The initial applications of an MDOF NES coupled in series to a primary structure that possesses more than 2 DOF can be found in Panagopoulos et al. [3] and Tsakirtzis et al. [4], in which *simultaneous* broadband resonant interactions of multiple modes of the NES with those of the primary system were detected. The topological structure of the intrinsic periodic orbits becomes enriched through higher codimension bifurcations [4]. This highly degenerate bifurcation structure of intrinsic periodic orbits contributes to the intensity of targeted energy transfers from the primary structure to the MDOF NES.

The robustness of instability suppression for the SDOF NES will be investigated further in Sec. II of this work, in which sets of Hopf and limit point cycle bifurcations in the three-dimensional parameter space of offset attachment, reduced velocity, and either mass ratio, damping coefficient, or essential nonlinearity are computed. Then, in Sec. III, the effect of an MDOF NES coupled in series to a wing is studied, to prove that this type of attachment can improve the robustness of instability suppression. A bifurcation analysis through a numerical continuation technique is performed to construct bifurcation sets in three-dimensional parameter space. A comparison of these bifurcation diagrams to those corresponding to an SDOF NES will provide design guidelines for optimality of NES performance. In particular, TET mechanisms for the MDOF NES will be investigated by studying nonlinear resonant interactions between the aeroelastic modes and multiple NES modes by means of wavelet transforms. An alternative, the MDOF NES coupled in parallel to the wing, will be considered in Sec. IV, in which the concentrated mass effect on LCO suppression will be indirectly demonstrated. Concluding remarks will be given in Sec. V.

II. SDOF NES and Robustness of Suppression

In this section, we revisit the study of the robustness of aeroelastic instability suppression in a rigid wing by applying the SDOF NES in

Lee et al. [1]. The equations of motion for the 2-DOF rigid wing model integrated with an SDOF NES as shown in Fig. 1 can be written as

$$
\begin{aligned}
&m\ddot{h} + S_\alpha \ddot{\alpha} + K_h(h + c_1 h^3) + qSC_{L,\alpha}(\alpha + \dot{h}/U) \\
&\quad + c_s(\dot{h} - d\dot{\alpha} - \dot{z}) + k_s(h - d\alpha - z)^3 = 0 \\
&I_\alpha \ddot{\alpha} + S_\alpha \ddot{h} + K_\alpha(\alpha + c_2\alpha^3) - qeSC_{L,\alpha}(\alpha + \dot{h}/U) \\
&\quad + dc_s(d\dot{\alpha} + \dot{z} - \dot{h}) + dk_s(d\alpha + z - h)^3 = 0 \\
&m_s \ddot{z} + c_s(\dot{z} + d\dot{\alpha} - \dot{h}) + k_s(z + d\alpha - h)^3 = 0
\end{aligned}
\tag{1}
$$

or, in nondimensional form,

$$
\begin{aligned}
&y'' + x_\alpha \alpha'' + \Omega^2 y + \xi_y y^3 + \mu C_{L,\alpha}\Theta(y' + \Theta\alpha) \\
&\quad + \epsilon\lambda(y' - \delta\alpha' - v') + C(y - \delta\alpha - v)^3 = 0 \\
&r_\alpha^2 \alpha'' + x_\alpha y'' + r_\alpha^2 \alpha + \xi_\alpha \alpha^3 - \gamma\mu C_{L,\alpha}\Theta(y' + \Theta\alpha) \\
&\quad + \delta\epsilon\lambda(\delta\alpha' + v' - y') + \delta C(\delta\alpha + v - y)^3 = 0 \\
&\epsilon v'' + \epsilon\lambda(v' + \delta\alpha' - y') + C(v + \delta\alpha - y)^3 = 0
\end{aligned}
\tag{2}
$$

where small motions and quasisteady aerodynamic forces are assumed. The authors acknowledge the simplicity and limited applicability of the aerodynamic model employed herein. However, it suffices for the proof of the energy sink concept for LCO suppression as demonstrated analytically, computationally, and experimentally [1,2]. Future efforts will be directed toward the transonic regime, for which unsteady aerodynamic effects cannot be neglected.

The robustness of instability suppression can be defined according to whether the three suppression mechanisms achieved by means of targeted energy transfers can be sustained in the presence of disturbances. Lee et al. [1] computed the steady-state amplitude ratio as follows:

$$
\frac{\text{Steady-state amplitude in rms with the NES}}{\text{Steady-state amplitude in rms without the NES}} \times 100(\%)
$$

with respect to a set of initial velocities in both the heave and pitch modes and for two different reduced velocities with two mass ratios of the NES.

These calculations, followed by a subsequent series of bifurcation analyses for fixed NES parameters, suggested that suppressing instability for the higher reduced velocities requires a larger NES mass. Here, we perform similar computations for the pitch amplitude ratio with the same wing parameters but, now, considering a negative offset (i.e., the NES attached close to the trailing edge of the wing) as well.

Figure 2 depicts the steady-state pitch amplitude ratio for a fixed reduced velocity ($\Theta = 0.9$) with respect to the same initial condition set as in Lee et al. [1] for two NES offsets (i.e., $\delta = \pm 0.9$). It was noted that negative offsets tend to exhibit better performance in suppressing instabilities, as can be verified from Fig. 2. With the same mass ratio, complete elimination of instability can be achieved

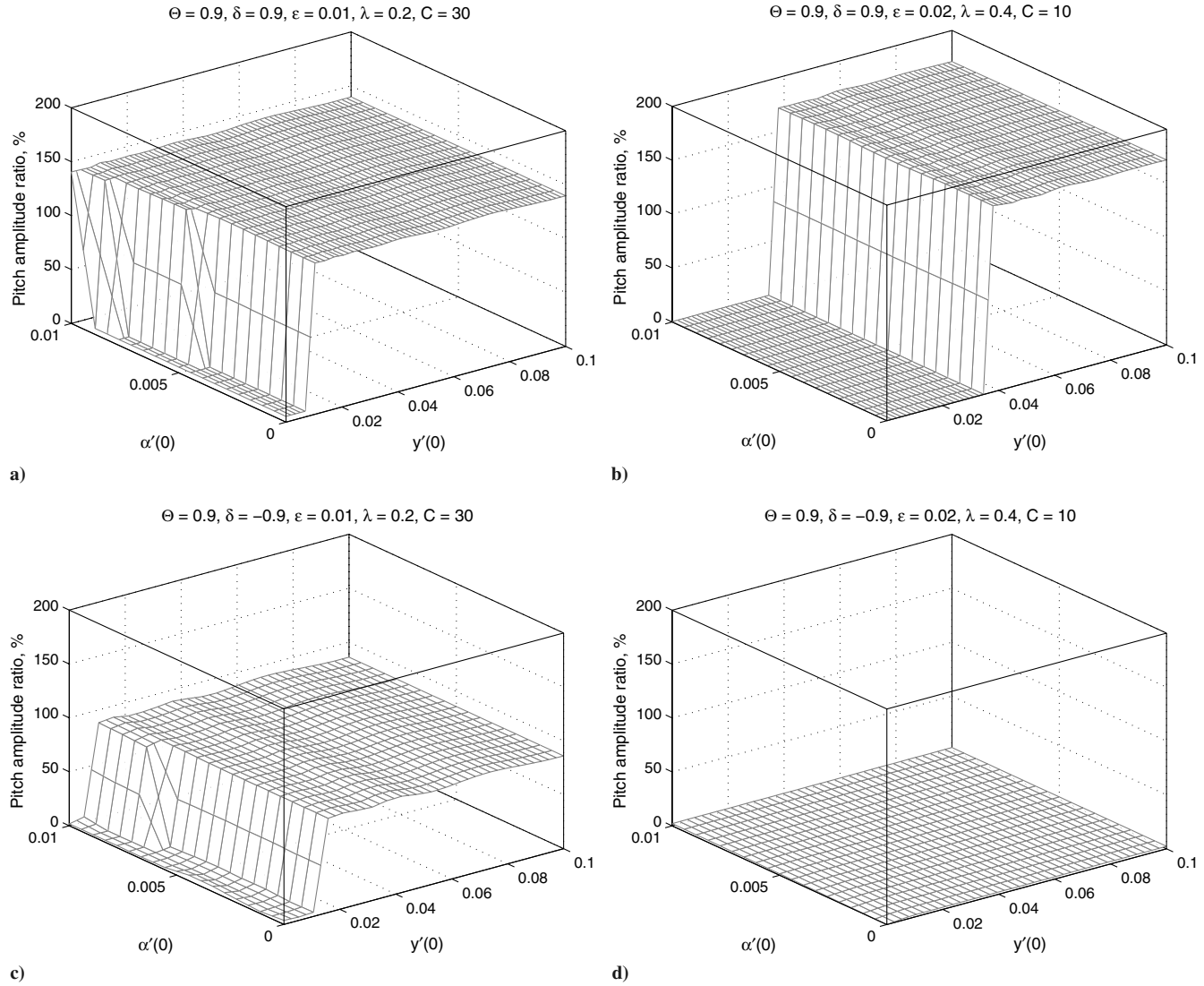

Fig. 2 The steady-state pitch amplitude ratio with respect to the initial condition set when the SDOF NES is used at the reduced speed.

for a larger set of initial conditions when an NES is attached with negative offset. Figure 2d demonstrates that complete elimination is possible over the whole domain of interest.

We superimpose the bifurcation diagrams from Lee et al. [1] in a single diagram by using a numerical continuation method, MatCont, which implements MATLAB® codes developed by Dhooge et al. [5] (Fig. 3a). This clearly illustrates the types of attachments that provide more robust suppression of instability. NES attachments with both positive and negative offsets basically delay the occurrence of LCO; the Hopf bifurcation points (Θ_H; squares in Fig. 3a) are located at reduced velocities higher than the linear flutter speed, $\Theta_F = 0.87$ [6]. For positive offset, the LPC bifurcation point (Θ_{LPC2}; triangles in Fig. 3a) near the pitch amplitude of 0.1 is far lower than Θ_H. Because of the unstable LCO branch between the two LPC bifurcation points (Θ_{LPC1} and Θ_{LPC2}), the stable trivial equilibrium between Θ_{LPC2} and Θ_H jumps to a stable LCO branch at a larger pitch amplitude under disturbances. However, for negative offset, Θ_{LPC2} occurs at higher reduced speeds than Θ_H, which implies that the stable trivial equilibrium and the partially suppressed LCOs at speeds less than Θ_{LPC2} will retain their steady state under any disturbances.

Figures 3a and 3b demonstrate robustness of the partial suppression and recurring burstouts and suppression mechanisms under a strong impulsive disturbance exerted on the heave mode at the steady state. Whereas partial suppression of instability is recovered after transients when $\Theta = 0.915$, the recurrent burstouts of instability when $\Theta = 0.95$ exhibit a jump to a stable LCO of larger amplitude. This is obvious from the bifurcation diagram. For $\Theta = 0.915$, there exist an unstable trivial equilibrium and small-amplitude stable LCO in the system with the NES attached at $\delta = -0.75$. However, when the reduced velocity increases to $\Theta = 0.95$, the system possesses two small-amplitude unstable LCOs (one occurs through NS bifurcation, the other through LPC bifurcation) and a large-amplitude stable LCO generated through a branch point cycle bifurcation (BPC; denoted by the asterisks in the diagram). Hence, it demonstrates that the bifurcation structure of LCOs, as well as the efficient nonlinear resonant interactions between the aeroelastic and NES modes as the underlying dynamic mechanisms, is critical to achieving robustness of instability suppression.

Being interested in the location of the LPC bifurcation point (Θ_{LPC2}) relative to the Hopf bifurcation (Θ_H), we extend the analysis

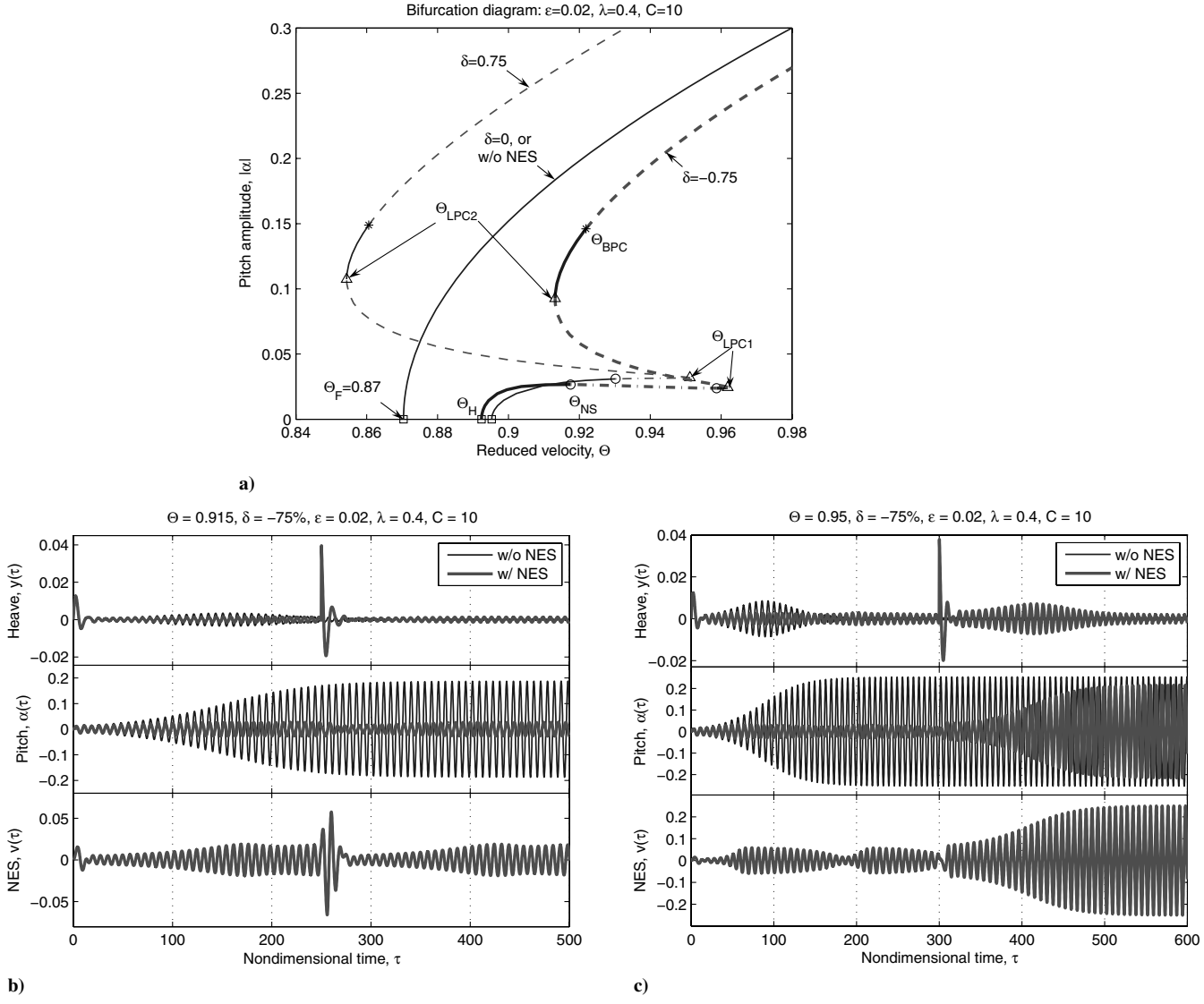

Fig. 3 Demonstration of robustness issue: a) bifurcation diagram (incomplete) with respect to Θ for the SDOF NES ($\epsilon = 0.02$, $\lambda = 0.4$, $C = 10$). Solid (dashed, dashed-dotted) lines indicate stable (unstable, quasiperiodic) LCO branches. Squares (circles, triangles, asterisks) indicate the Hopf (Neimark–Sacker, limit point cycle, branch point cycle) bifurcation points; jump phenomena (i.e., nonrobust suppression of instability) occurs from one stable LCO branch to another due to an impulsive disturbance to only the heave mode, that is, additional $20 \times y'(0)$ is imposed at $\tau = 250$ for b) $\Theta = 0.915$ and at $\tau = 300$ for c) $\Theta = 0.95$.

in Lee et al. [1] to the computation of the bifurcation sets in three-dimensional parameter space. Along the LCO branches with the reduced velocity Θ as the continuation parameter, bifurcations of the LCOs with an SDOF NES generally occur from Hopf bifurcation followed sequentially by NS_1, NS_2, LPC_1, LPC_2, and BPC bifurcations. As far as the MDOF NES is concerned, these bifurcations, except for the LPC bifurcation, become more degenerate or high codimensional (note that the LPC bifurcation always involves nonzero imaginary eigenvalues). For example, Hopf is detected as double Hopf, generalized Hopf, or neutral saddle, and NS as neutral saddle. These degenerate bifurcations will not be of interest in this study. The characteristics of each bifurcation surface in terms of enhancing the robustness of instability suppression are summarized as follows:

1) The Hopf bifurcation of a trivial equilibrium of the aeroelastic system gives rise to a periodic solution called an LCO. A comparison of the Hopf bifurcation points with and without an NES indicates how much the linear flutter speed can be delayed or improved.

2) The LPC bifurcation is more often called saddle-node bifurcation. The LPC bifurcation denoted by LPC_1 implies the critical point, above which any type of suppressed LCO (regardless of robustness) can no longer be observed. Another LPC bifurcation point (LPC_2) contributes to the lower limit of the unstable LCO branch. The robustness of instability suppression by using the SDOF NES can be determined by the location of the LPC_2 bifurcation point relative to the Hopf bifurcation.

3) The NS bifurcation is the Hopf bifurcation of an LCO, resulting in another period, so that the resulting LCO exhibits quasi periodicity. Therefore, the NS bifurcation is responsible for the recurrent burstouts and suppressions of instability and generally occurs in the branch between the Hopf and LPC_1 bifurcation points.

4) The BPC bifurcation, which is a codimension-2 bifurcation of a limit cycle, occurs after the LPC_2 bifurcation point along the continuation of limit cycles. This BPC bifurcation is not of interest in this study and will not be analyzed further.

Figures 4a–4c present bifurcation sets for the SDOF NES in the three-dimensional parameter spaces $(\epsilon, \delta, \Theta)$, $(\lambda, \delta, \Theta)$, and (C, δ, Θ), respectively. Construction of these 3-D bifurcation sets can be understood in the following way. (The same principles are applied to understanding those for the MDOF NES as depicted in Fig. 11.) In the bifurcation diagram of Fig. 3a, the NES parameters are fixed, that is, $\epsilon = 0.02$, $\lambda = 0.4$, $C = 10$. Then, consider a plane $\epsilon = 0.02$ in Fig. 4a, resulting in Fig. 5 in which three curves can be identified from the intersections between this plane of constant mass ratio and the three bifurcation sets (Hopf and two LPC bifurcations). If the bifurcation behavior when the NES is attached at an offset $\delta = \mp 0.75$ is of interest, another plane of a constant offset can be imposed (Figs. 5a and 5b, respectively).

Once these two planes of interest are constructed in the 3-D bifurcation sets, the z axis starting at the Hopf bifurcation point Θ_H above $\epsilon = 0.02$ no longer represents a mass ratio but rather

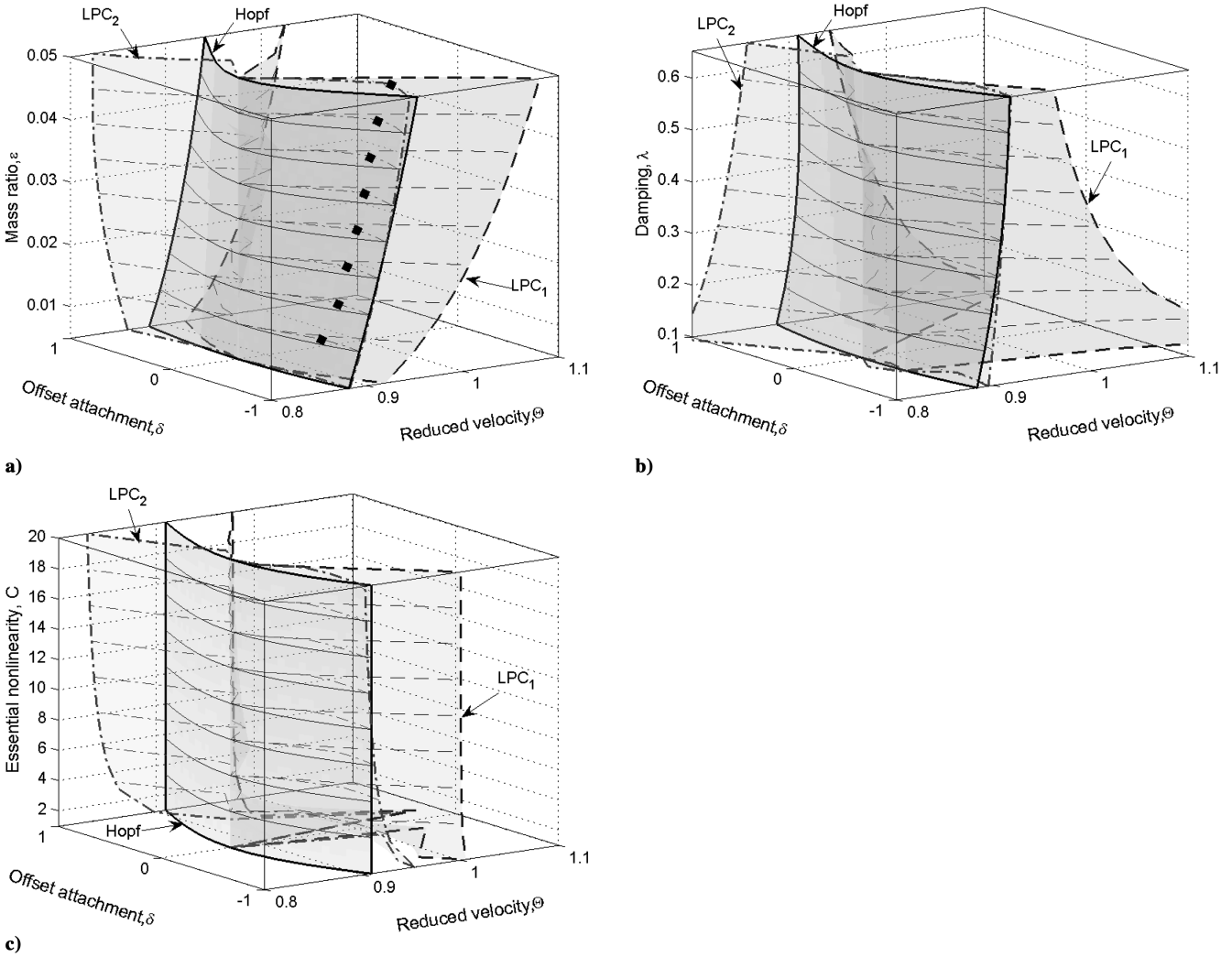

Fig. 4 Bifurcation set for the 2-DOF rigid wing with the SDOF NES: a) effect of the mass ratio (ϵ) with $\lambda = 0.4$, $C = 10$ (diamonds on the LPC_2 surface imply the locations of optimal offset for enhancing the robustness of instability suppression); b) effect of damping (λ) with $\epsilon = 0.02$, $C = 10$; and c) effect of essential nonlinearity (C) with $\epsilon = 0.02$, $\lambda = 0.4$.

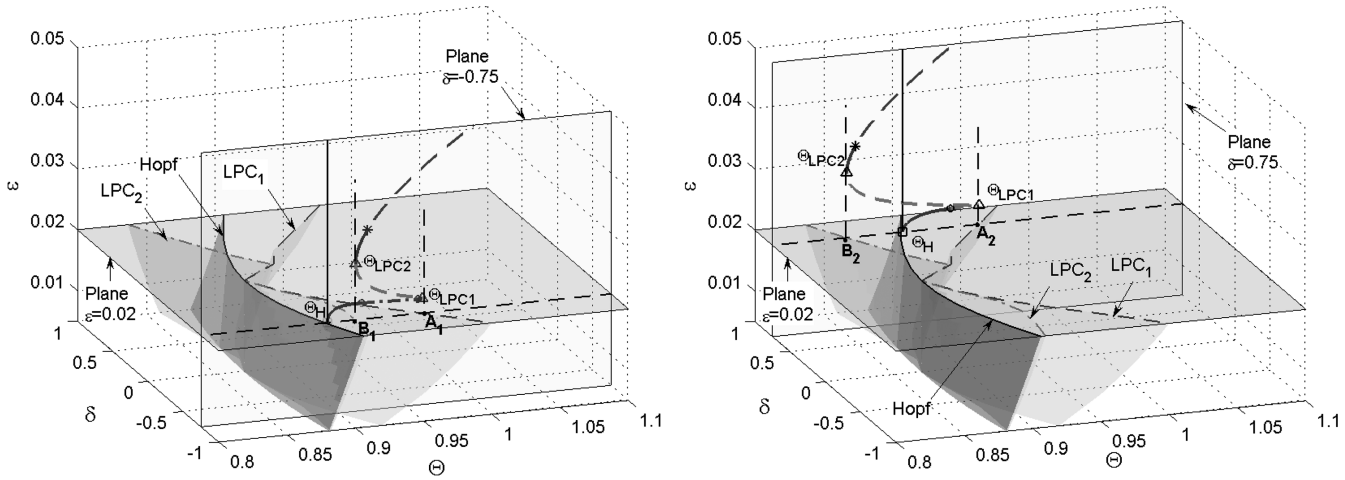

a) $\delta = -0.75$ **b)** $\delta = 0.75$

Fig. 5 Understanding of the 3-D bifurcation sets when $\epsilon = 0.02$.

the LCO amplitude. Then, the bifurcation diagram in Fig. 3a can be drawn on the planes $\delta = \mp 0.75$. The two dashed vertical lines passing through Θ_{LPC1} and Θ_{LPC2} correspond exactly to the points $A_{1,2}$ and $B_{1,2}$, respectively. $A_{1,2}$ ($B_{1,2}$) are found as the intersection of the planes, $\epsilon = 0.02$, $\delta = \mp 0.75$, and the LPC_1 (LPC_2) bifurcation surface. With this construction, condensed information about bifurcation behavior in the 3-D parameter space is more easily understood.

Note that, to clarify the robustness features, the NS and BPC bifurcation surfaces are not included and further codimension-2 or higher bifurcation analysis is not performed. Recall that, for the SDOF NES, a zero offset attachment does not significantly affect aeroelastic responses; LCO branches including bifurcation behavior are almost coincident. The two LPC bifurcation surfaces coalesce into the Hopf bifurcation surface at δ very close to zero.

In the following, we observe effects of the NES mass ratio (ϵ), damping (λ), and essential nonlinearity coefficient (C) on instability suppression, with the other two parameters being offset attachment (δ) and reduced velocity (Θ).

1) *Mass Ratio* (Fig. 4a): The NES mass ratio contributes most significantly to the delay of Hopf bifurcation, contrary to the general belief that the effect of damping is greater. As the mass ratio increases along with the offset attachment away from the elastic axis, the Hopf and LPC bifurcations exhibit a monotonic increment in corresponding reduced velocity values.

In terms of the robustness of instability suppression, which is characterized by the location of LPC_2 relative to the Hopf point, an optimal interval of offset attachment exists for each mass ratio. That is, if the SDOF NES is attached too far away from the elastic axis, then LPC_2 occurs very close to the Hopf point for negative offset. Even worse, it can exist at a reduced velocity smaller than the Hopf point for positive offset. As was conjectured in Lee et al. [1], if the NES possesses a larger mass, the robustness of instability suppression improves within the optimal offset interval. The points denoted by a diamond in Fig. 4a imply the optimal offset for the robustness of instability suppression.

LCO surfaces (in the pitch mode) for six values of mass ratio are presented in Fig. 6. As the mass ratio increases, the LPC bifurcation curves occur at higher pitch amplitudes. This indirectly explains why the robust suppression of instability is barely observed with a very small NES mass. First of all, the Hopf bifurcation curve for a small NES mass (Fig. 6a) appears almost flat along the offset direction, which means no improvement of the linear flutter speed. Secondly, partially suppressed LCO branches exist, but their intervals in the reduced velocity direction are short. Moreover, LCOs with small amplitudes on those branches are vulnerable to disturbances, after which the aeroelastic responses can jump to LCOs of large amplitudes. Except for these LCO branches exhibiting partial instability suppression and recurring burstouts and suppressions of instability, the overall shape of LCO branches appears close to the LCO branch for the aeroelastic response with no NES applied.

2) *Damping* (Fig. 4b): Although not as significant as the mass ratio, increasing the damping coefficient improves the flutter speed. The overall robustness behavior looks similar to that obtained with an increasing mass ratio. That is, there exist optimal intervals of offset attachment, and negative offset provides better performance.

As depicted in Fig. 7, the LPC bifurcation curves with increasing damping are located at the larger LCO amplitudes. Very low damping (Fig. 7a) results in inefficient energy dissipation in the NES of the energy input from the flow to the wing, so that it tends to yield nonrobust suppression mechanisms over the reduced velocities of interest.

3) *Essential Nonlinearity* (Fig. 4c): The bifurcation sets (Hopf and LPC) are almost insensitive to the coefficient of the essential nonlinearity. The robustness of instability suppression is not much affected by the essential nonlinearity if its magnitude is sufficiently large. The main role of the essential nonlinearity is to provide broadband nonlinear resonant interaction between the primary and NES subsystems.

Except for the case when $C = 1$ (i.e., C is very small), Fig. 8 supports this observation. All the LCO surfaces appear similar to each other as the magnitude of the essential nonlinearity increases. A small distinction is that the LPC bifurcation curves are suppressed to lower pitch amplitudes as C increases.

Along with the dynamic mechanisms of instability suppression in Lee et al. [1], the bifurcation analysis was extended to the three-dimensional parameter space in this section so that dependence of the robustness on the NES parameters (mass ratio, damping, and essential nonlinearity) is clarified. As a method to enhance this robustness of instability suppression, MDOF NESs will be considered in Sec. III. Panagopoulos et al. [3] tried to explain TETs with an MDOF NES in terms of underlying Hamiltonian dynamics (i.e., on the frequency-energy domain) and also by using a perturbation analysis. In this study, bifurcation analysis in conjunction with numerical continuation will clarify robustness enhancement with the MDOF NES and targeted energy transfers.

III. MDOF NES and Robustness Enhancement

In this section, we introduce the MDOF NES in series coupling with the 2-DOF rigid wing model to improve the robustness of suppression of aeroelastic instabilities. The enriched dynamics caused by highly singular bifurcations such as generalized Hopf bifurcation [7] are expected to yield more efficient broadband

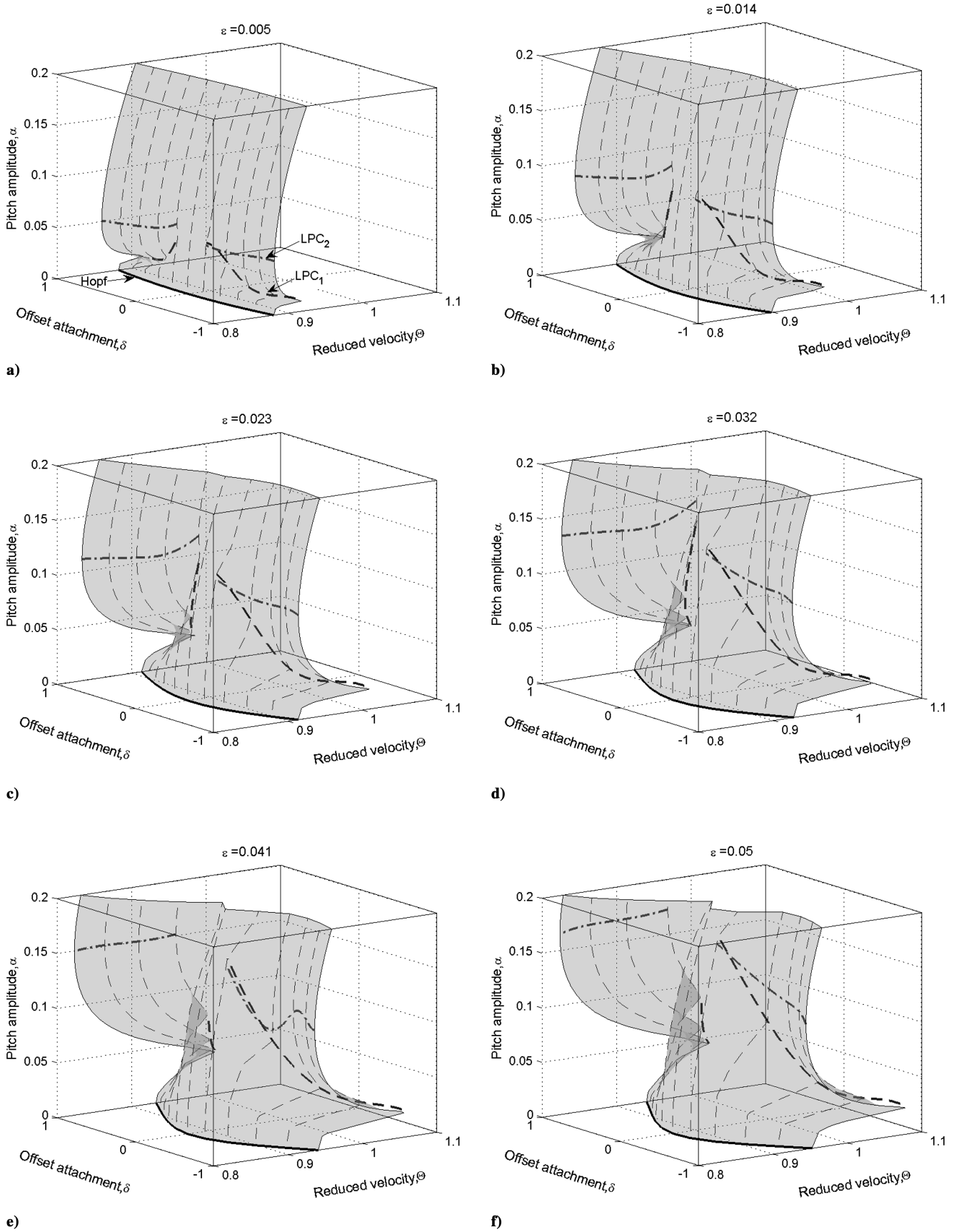

Fig. 6 Surfaces of LCO branches with respect to the mass ratio ϵ when the SDOF NES is attached to the 2-DOF rigid wing ($\lambda = 0.4$, $C = 10$). The bold solid (dashed, dashed-dotted) line denotes the Hopf (LPC_1, LPC_2) bifurcation curve.

targeted energy transfers for enhancing the robustness of instability suppression.

A. MDOF NES Configuration in Series Coupling

Figure 9 depicts the 2-DOF rigid wing, to which an MDOF NES is coupled in series. Assuming small motions, the equations of motion for this system can be written as

$$
\begin{aligned}
&m\ddot{h} + S_\alpha\ddot{\alpha} + K_h(h + c_1h^3) + qSC_{L,\alpha}(\alpha + \dot{h}/U) \\
&\quad + k(h - d\alpha - z_1) = 0 \\
&I_\alpha\ddot{\alpha} + S_\alpha\ddot{h} + K_\alpha(\alpha + c_2\alpha^3) - qSeC_{L,\alpha}(\alpha + \dot{h}/U) \\
&\quad + dk(d\alpha + z_1 - h) = 0 \\
&\tfrac{1}{3}m_s\ddot{z}_1 + c_s(\dot{z}_1 - \dot{z}_2) + k(z_1 + d\alpha - h) + k_s(z_1 - z_2)^3 = 0 \\
&\tfrac{1}{3}m_s\ddot{z}_2 + c_s(\dot{z}_2 - \dot{z}_1) + c_s(\dot{z}_2 - \dot{z}_3) + k_s(z_2 - z_1)^3 \\
&\quad + \tfrac{1}{50}k_s(z_2 - z_3)^3 = 0 \\
&\tfrac{1}{3}m_s\ddot{z}_3 + c_s(\dot{z}_3 - \dot{z}_2) + \tfrac{1}{50}k_s(z_3 - z_2)^3 = 0
\end{aligned}
\tag{3}
$$

or, in nondimensional form (Lee et al. [1]),

$$
\begin{aligned}
&y'' + x_\alpha\alpha'' + \Omega^2 y + \xi_y y^3 + \mu C_{L,\alpha}\Theta(y' + \Theta\alpha) \\
&\quad + C_1(y - \delta\alpha - v_1) = 0 \\
&r_\alpha^2\alpha'' + x_\alpha y'' + r_\alpha^2\alpha + \xi_\alpha\alpha^3 - \gamma\mu C_{L,\alpha}\Theta(y' + \Theta\alpha) \\
&\quad + \delta C_1(\delta\alpha + v_1 - y) = 0 \\
&\tfrac{1}{3}\epsilon v_1'' + \epsilon\lambda(v_1' - v_2') + C_1(v_1 + \delta\alpha - y) + C(v_1 - v_2)^3 = 0 \\
&\tfrac{1}{3}\epsilon v_2'' + \epsilon\lambda(v_2' - v_1') + \epsilon\lambda(v_2' - v_3') + C(v_2 - v_1)^3 \\
&\quad + \tfrac{1}{50}C(v_2 - v_3)^3 = 0 \\
&\tfrac{1}{3}\epsilon v_3'' + \epsilon\lambda(v_3' - v_2') + \tfrac{1}{50}C(v_3 - v_2)^3 = 0
\end{aligned}
\tag{4}
$$

Some features of the MDOF NES are noted as follows:

1) The total mass of the MDOF NES is the same as the SDOF NES of the Sec. II. That is, a single mass (ϵ) in the SDOF NES is divided into the three equal masses ($\epsilon/3$) in the MDOF NES.

2) The linear coupling stiffness between the wing structure and mass 1 (shown in Fig. 9) plays a role as the passage for energy transfers between the aeroelastic and NES modes. For a weaker linear coupling, the NES will exhibit better performance (i.e., better targeted energy transfers).

3) The first essentially nonlinear coupling between masses 1 and 2 should be greater than that between masses 2 and 3. Consistent with previous research [3,4], a factor of 0.02 is adopted as the optimal value of the coefficient of the second essential nonlinearity.

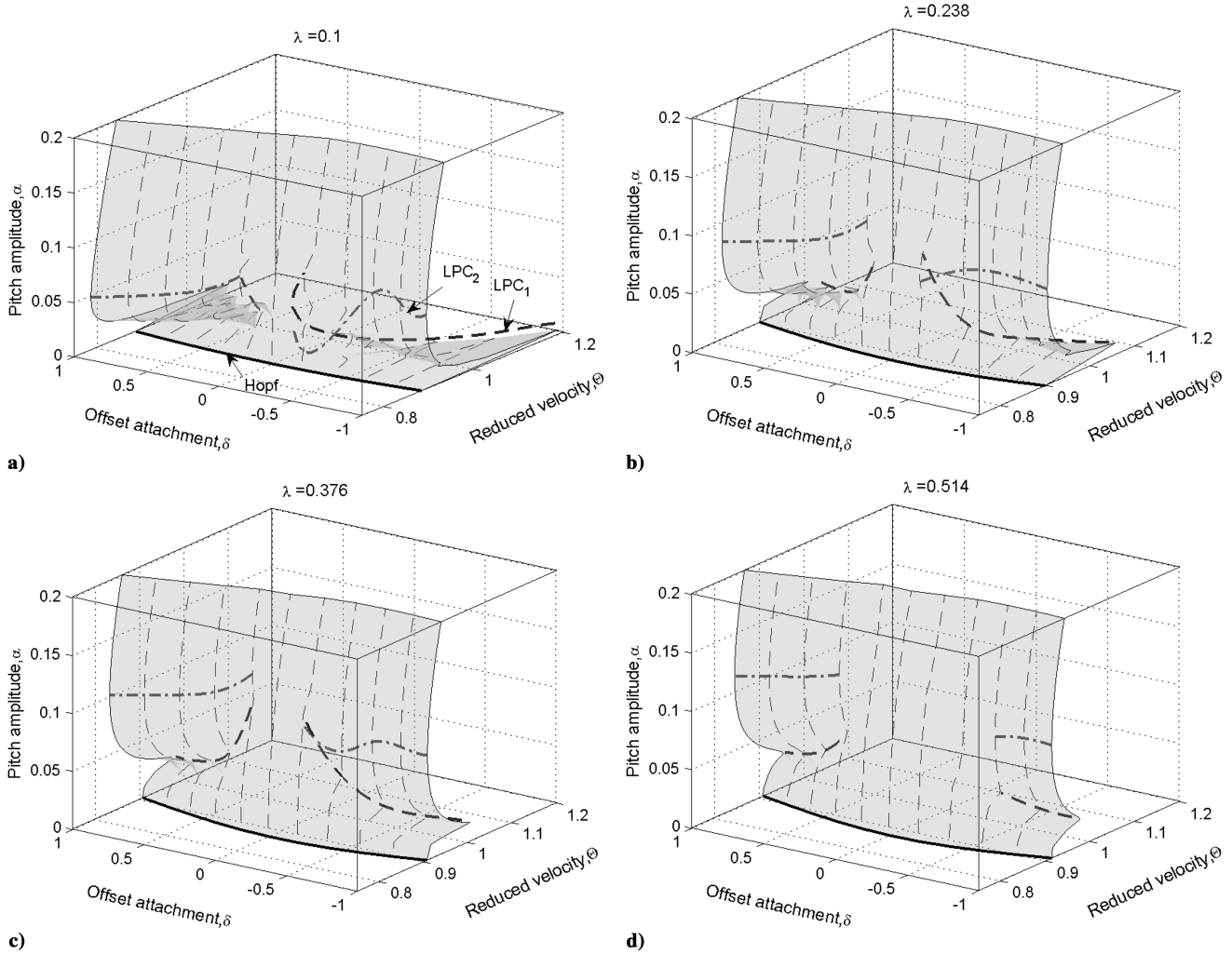

Fig. 7 Surfaces of LCO branches with respect to the damping λ when the SDOF NES is attached to the 2-DOF rigid wing ($\epsilon = 0.02$, $C = 10$). The bold solid (dashed, dashed-dotted) line denotes the Hopf (LPC_1, LPC_2) bifurcation curve.

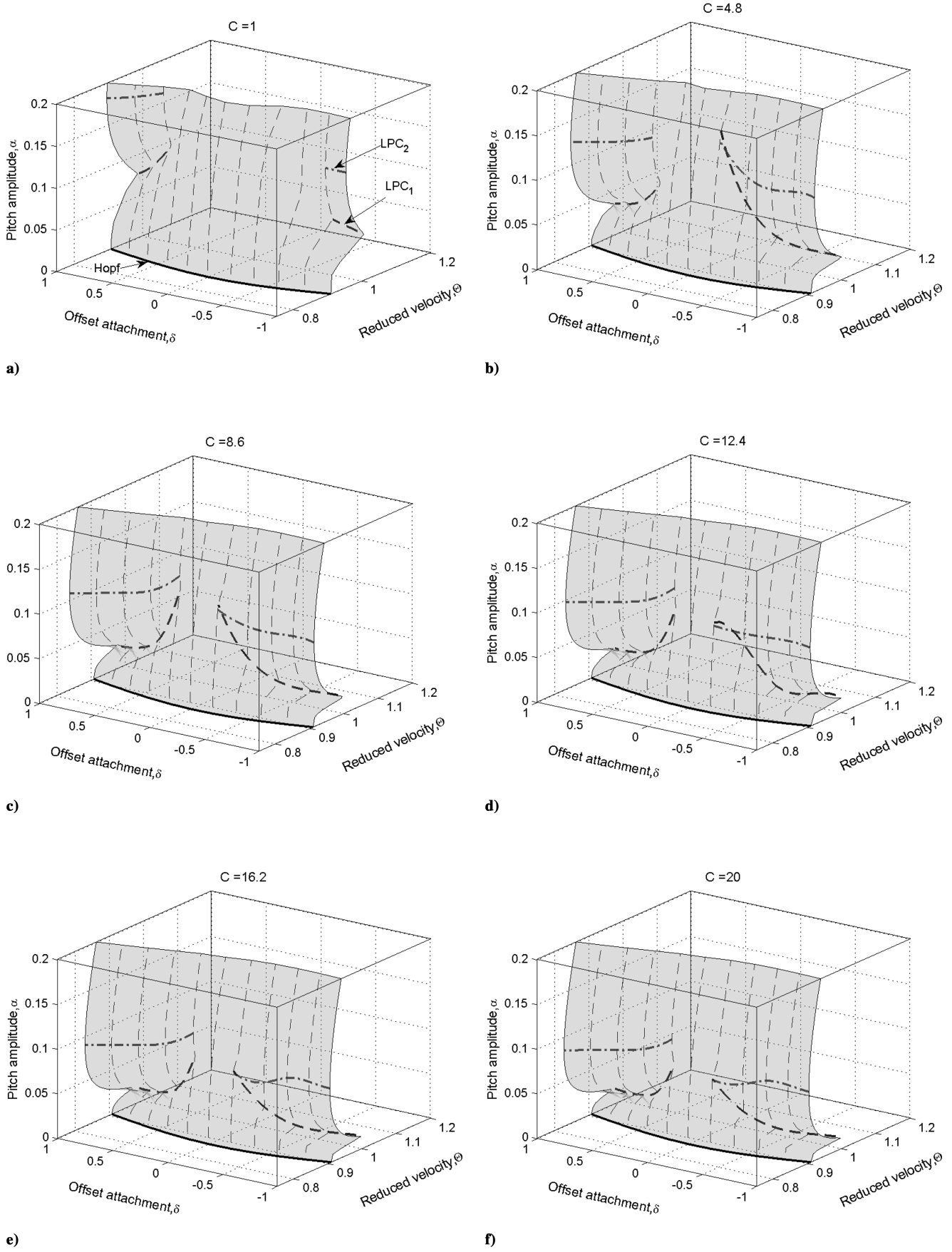

Fig. 8 Surfaces of LCO branches with respect to the essential nonlinearity *C* when the SDOF NES is attached to the 2-DOF rigid wing ($\epsilon = 0.02$, $\lambda = 0.4$). The bold solid (dashed, dashed-dotted) line denotes the Hopf (LPC_1, LPC_2) bifurcation curve.

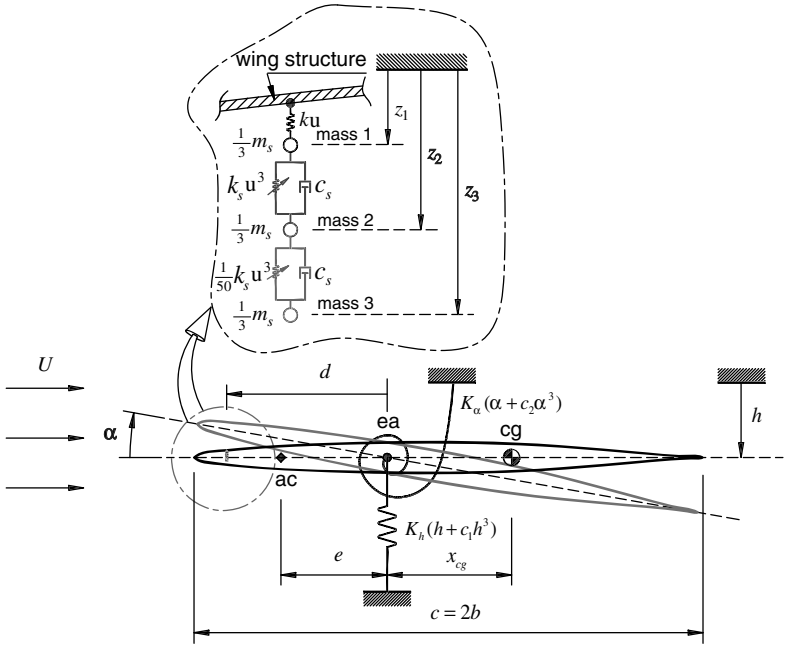

Fig. 9 Application of the MDOF NES in series coupling for the 2-DOF rigid wing.

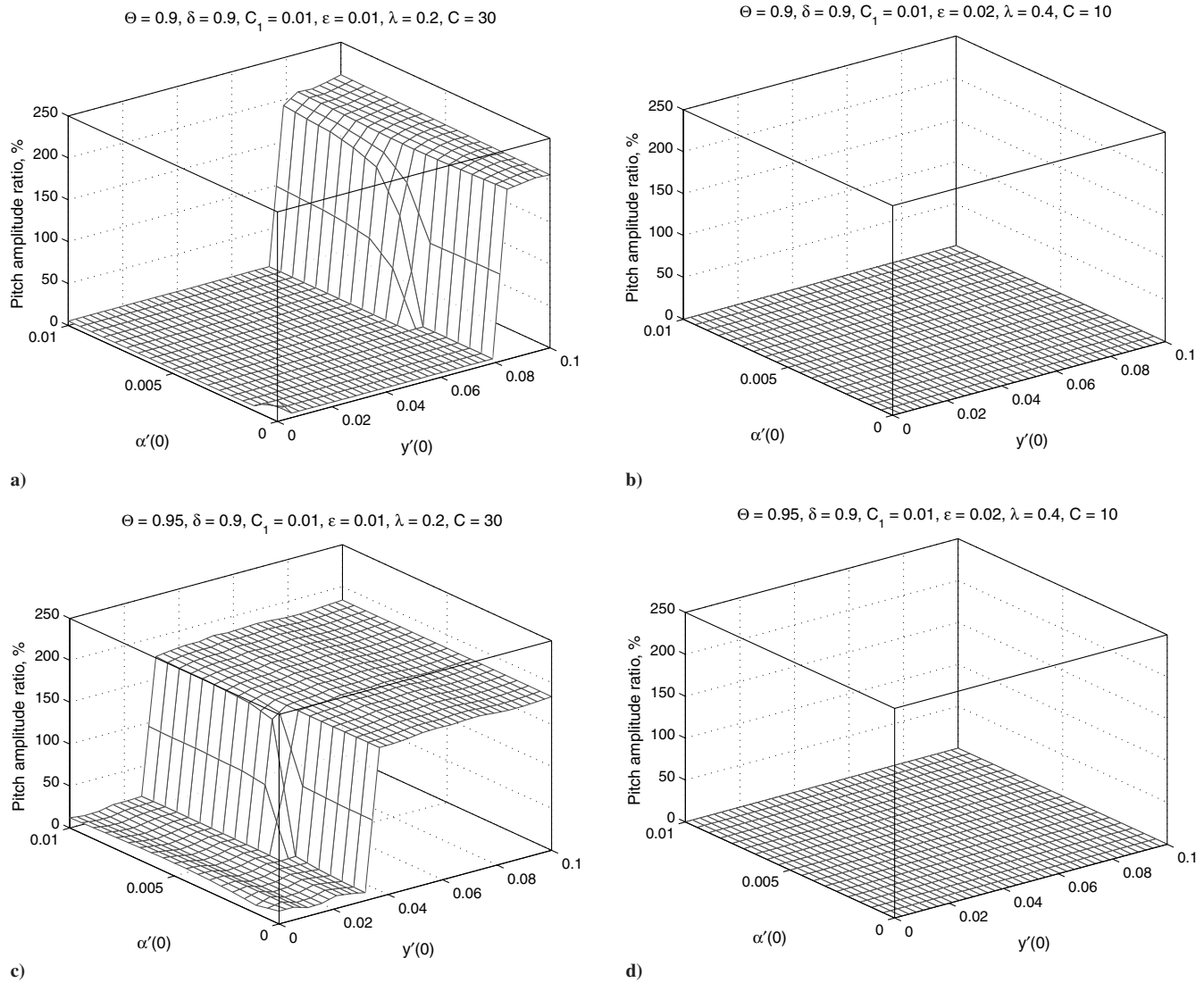

Fig. 10 Dependence of the steady-state pitch amplitude on the initial conditions when the series MDOF NES with a weak linear coupling is used.

For a comparison with the calculations in Lee et al. [1] (and also with Fig. 2), we compute the steady-state pitch amplitude ratio as another way of demonstrating the robustness enhancement (Fig. 10). Observe that the domain of initial conditions in which the complete suppression of instability can be achieved becomes larger with a very small NES mass (i.e., $\epsilon = 0.01$, 1% of the total wing mass; see Figs. 10a and 10c). The mass ratio $\epsilon = 0.02$ can completely eliminate instability over the whole domain of interest, even for the reduced velocity $\Theta = 0.95$, which is a relatively high-speed flow that produces large-amplitude LCOs (above 0.25 rad or 15 deg in the pitch mode) with no NES applied.

All three suppression mechanisms defined in Lee et al. [1] can be identified. However, as will become apparent from the bifurcation analysis, the action of the MDOF NES in series coupling tends to suppress the occurrence of the Neimark–Sacker bifurcation. As a result, the first suppression mechanism, recurrent burstouts and suppressions of instability, rarely occurs. We suspect that the MDOF NES renders the NS bifurcation highly degenerate, for example, neutral saddle singularity [7], at which a numerical continuation method sometimes fails to further compute an LCO branch. This implies that partial or complete suppression of aeroelastic instabilities will be the main suppression mechanisms observed with the MDOF NES in series coupling.

B. Bifurcation Analysis

A numerical continuation technique [5] was used to construct bifurcation sets that are important for understanding the robustness enhancement with the MDOF NES. We consider two cases for the linear coupling stiffness: $C_1 = 0.1$ (stronger) and $C_1 = 0.01$ (weaker). Basically, the overall MDOF NES parameters are the same as those for the SDOF NES in Sec. II.

1. *Strong Linear Coupling Stiffness*

The left column of Fig. 11 depicts bifurcation sets for the stronger linear coupling stiffness with respect to the (overall) mass ratio, damping coefficient, and essential nonlinearity, respectively. The corresponding LCO surfaces for selected parameters are presented in Figs. 12–14.

We note that the Hopf bifurcation surfaces for the MDOF NES with a stronger linear coupling stiffness appear similar to those for the SDOF NES configuration as the mass ratio, damping, and essential nonlinearity vary. That is, the reduced velocity for the Hopf bifurcation monotonously increases for a fixed offset as the mass ratio increases and is almost insensitive to variations of the damping and essential nonlinearity. This is because mass 1 will behave as a rigid body together with the wing structure as the linear coupling becomes stiffer (i.e., stronger C_1). The strong linear coupling may possess strong linear resonant interaction and does not provide a path for efficient broadband targeted energy transfers between the two oscillators. Nonetheless, there is still an improvement in delaying the occurrence of the Hopf bifurcation when an MDOF NES is used, even with zero offset.

This monotonous behavior of the Hopf bifurcation surface with respect to the total mass ratio simply means that the larger NES mass provides better suppression of instability with the MDOF NES in series coupling with a strong linear coupling stiffness (Fig. 11a). The generation of the LPC bifurcations relative to the Hopf bifurcation renders this feature clearer. Both the LPC_1 and LPC_2 bifurcations for large offsets are located at reduced velocities higher than the Hopf bifurcation point, staying close to each other. This implies that the unstable LCO branch between the two LPC points exists in a short interval of the reduced velocity, so that the overall shape of the LCO branch appears as a curve with almost no turning points (Fig. 12).

The location of the LPC_2 point becomes higher than the Hopf bifurcation point as the mass ratio increases. The interval between these two bifurcation points corresponds to the reduced velocity in which one observes the robust suppression of instability. This almost monotonous, linear dependence of the Hopf bifurcation on the mass ratio may not be attractive for practical applications for which light weight is desirable.

The Hopf bifurcation mostly occurs as supercritical, that is, the stable LCOs are generated above the Hopf bifurcation point, below which there exists only a stable trivial equilibrium (Fig. 12). However, the Hopf bifurcation near the zero offset generates subcritical LCOs in a very short interval of reduced velocity (for example, at $\delta = -0.2$ in Figs. 11a–11c). The LPC_1 points are aligned vertically for all NES parameters at that offset, and they hardly affect the overall robustness of instability suppression. The LCO surfaces in Fig. 12 support these arguments. For example, similar to the SDOF NES, the LPC bifurcation occurs at a higher amplitude as the mass ratio increases. The LPC points tend to move away from the zero offset for a larger mass ratio.

The larger damping pushes the LPC bifurcation points to larger offsets (Fig. 13). The high damping also suppresses the occurrence of bifurcations of the LCOs and makes the LCO branches simpler. That is, the two LPC bifurcation points merge at larger offsets as the damping increases. Thus, the optimal intervals of offset for robust instability suppression can be found for smaller damping coefficients. Figure 11b depicts the bifurcation sets in $(\Theta, \delta, \lambda)$ space. As in the case of the SDOF NES, the Hopf surface exhibits less dependence on the magnitude of the damping compared with the total mass ratio ϵ.

Whereas the Hopf bifurcation surface still exhibits insensitivity to changes in the essential nonlinearity (Fig. 11c), the LPC bifurcations behave exactly the opposite of the damping increments as the essential nonlinearity increases. In other words, they become separated from each other for large offsets as C increases. The larger essentially nonlinear stiffness induces the two LPC bifurcation points at a lower LCO amplitude, which are attracted to the zero offset to form the LPC bifurcation curves in a larger interval of the offset (Fig. 14).

Similar to the SDOF NES, the negative offset provides better performance in suppressing instability for the MDOF NES in series coupling with a stronger linear coupling stiffness; further, the instability suppression will be robust (cf. Lee et al. [1]).

2. *Weak Linear Coupling Stiffness*

Unlike the stronger linear coupling stiffness, the weaker one removes the monotonous dependence of the Hopf bifurcation on the mass ratio, creating an optimal NES parameter in which Hopf bifurcation occurs at higher reduced velocities (Fig. 11d). The optimal mass ratio can be found near $\epsilon = 0.02$ only in terms of making LCOs occur at a higher reduced speed. Then, the location of the LPC bifurcation point with respect to the Hopf bifurcation dictates the robustness of instability suppression. The single LPC point lower than the Hopf point implies a subcritical Hopf bifurcation.

It is interesting to note that, around the optimal mass ratio, most of the LPC bifurcations occur at lower reduced velocities than the Hopf points for negative offsets and at higher reduced velocities for positive offsets. This behavior appears for varying damping and essential nonlinearity as well, that is, most of the LPC bifurcations occur at the reduced speed lower (higher) than the Hopf bifurcation point for negative (positive) offsets. Moreover, the separation between the LPC_1 and LPC_2 bifurcation points is maximized near the mass ratio at which the optimal delay of Hopf bifurcations can be achieved. This means that the robustness of instability suppression may not be enhanced at the optimal mass ratio.

Figure 15 depicts the LCO surfaces by selectively increasing the mass ratio of the MDOF NES in series coupling with a weak linear coupling stiffness. Comparing the Hopf bifurcation curves for $\epsilon = 0.014$ and $\epsilon = 0.023$ (Figs. 15b and 15c, respectively), $\epsilon = 0.023$ is the optimal mass ratio in terms of placing the Hopf bifurcation at higher reduced velocities. However, these Hopf bifurcations are subcritical, that is, the LPC bifurcation points are generated at lower reduced velocities. On the other hand, the mass ratio $\epsilon = 0.014$ delays the Hopf bifurcation point less, and all the Hopf bifurcations are supercritical with the LPC points greater than the Hopf points.

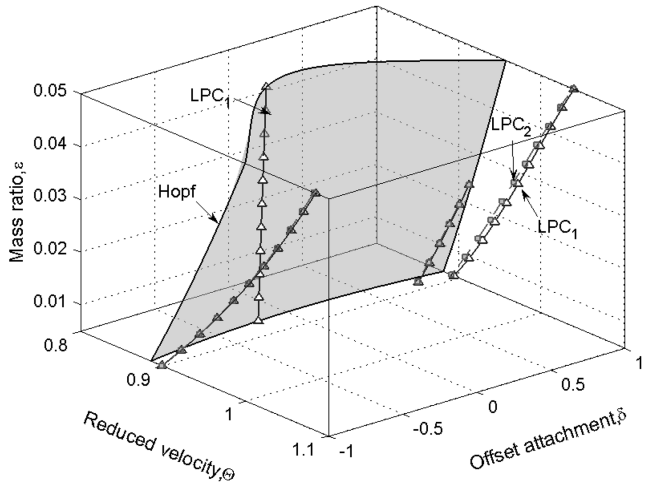

a)

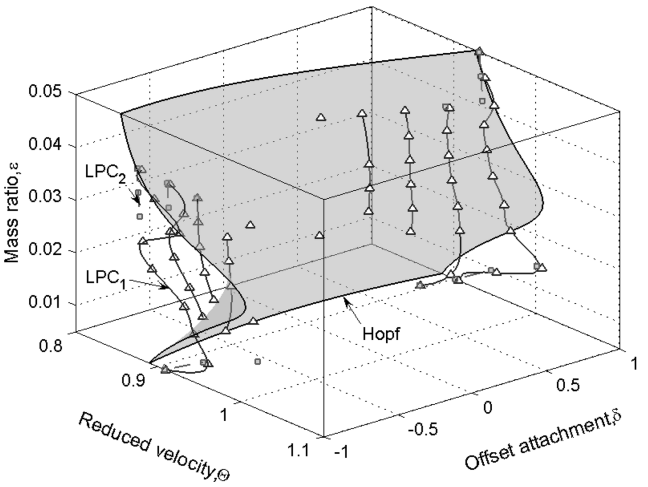

d)

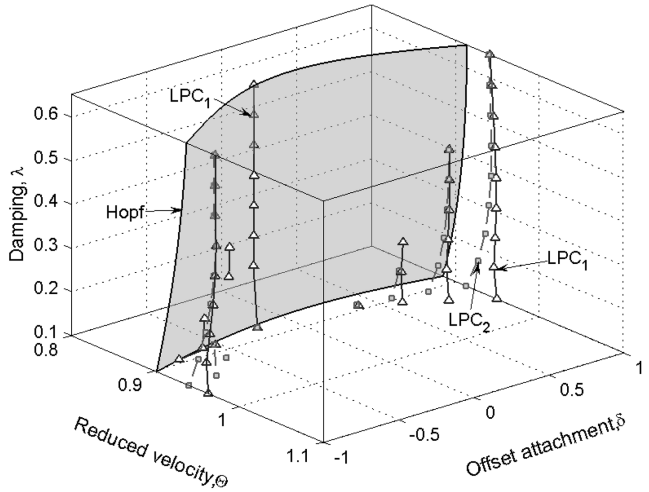

b)

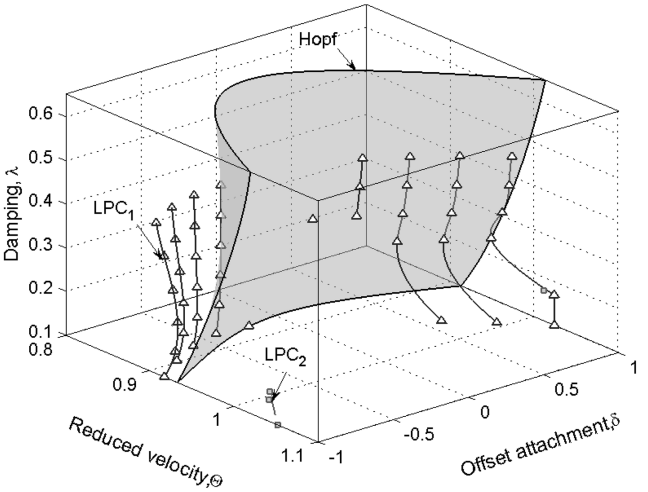

e)

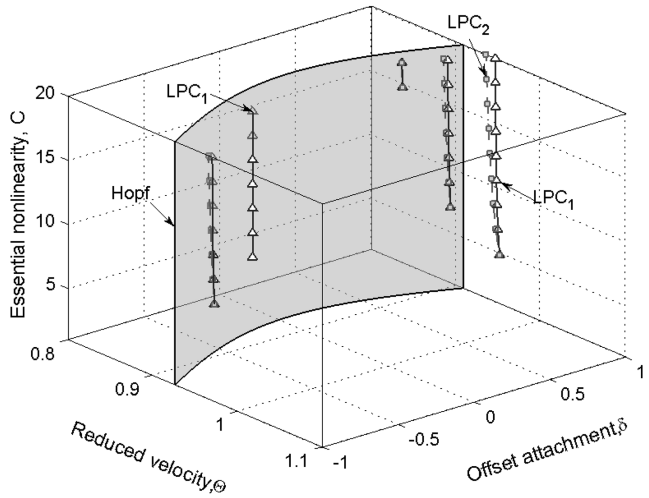

c)

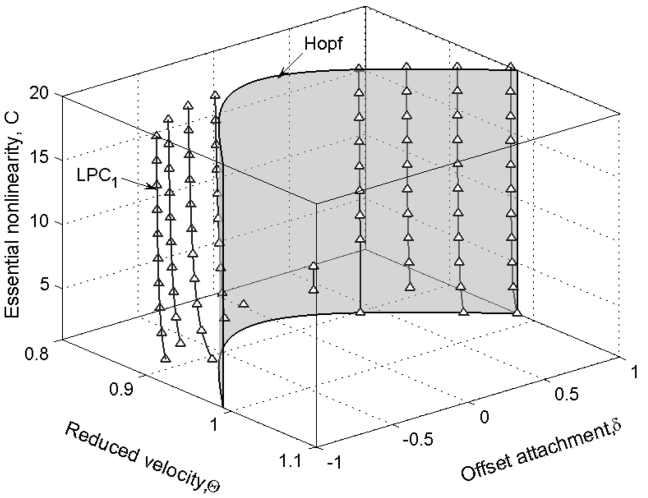

f)

Fig. 11 Bifurcation set for the 2-DOF rigid wing with the series MDOF NES in strong ($C_1 = 0.1$, left column) and weak ($C_1 = 0.01$, right column) linear couplings: Effects of a), d) mass ratio ϵ with $\lambda = 0.4$, $C = 10$; b), e) damping λ with $\epsilon = 0.02$, $C = 10$; and c), f) essential nonlinearity C with $\epsilon = 0.02$, $\lambda = 0.4$. The LPC_1 bifurcation points are denoted by triangles (connected with a solid line) and the LPC_2 bifurcation points by squares (connected with a dashed line).

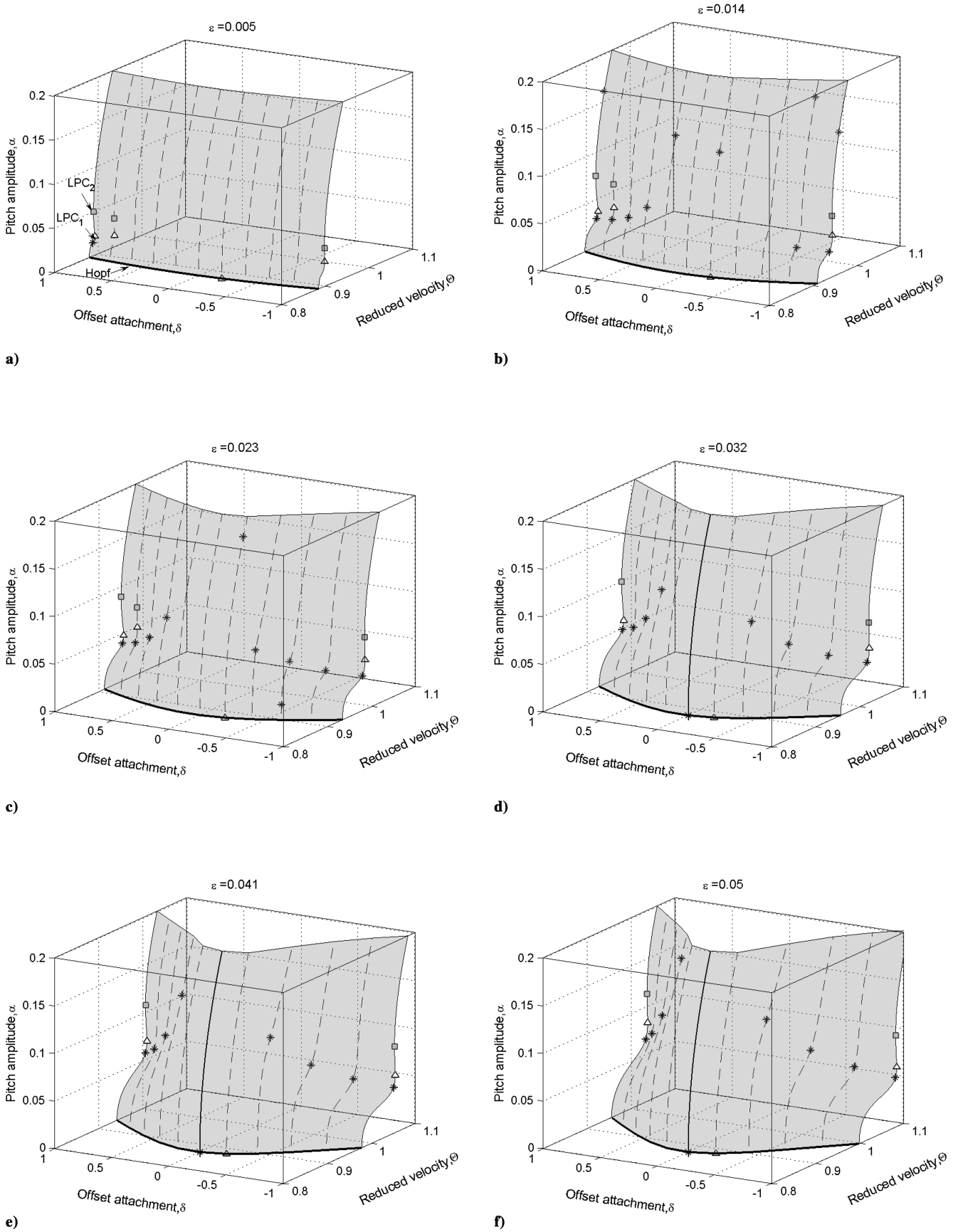

Fig. 12 Surfaces of LCO branches with respect to the mass ratio ϵ when the series MDOF NES with strong linear coupling is attached to the 2-DOF rigid wing ($\lambda = 0.4, C = 10$). The bold solid line denotes the Hopf bifurcation curve. The triangle (square) indicates the LPC_1 (LPC_2) bifurcation point. The asterisks denote degenerate bifurcation points such as neutral saddle or "generalized Hopf."

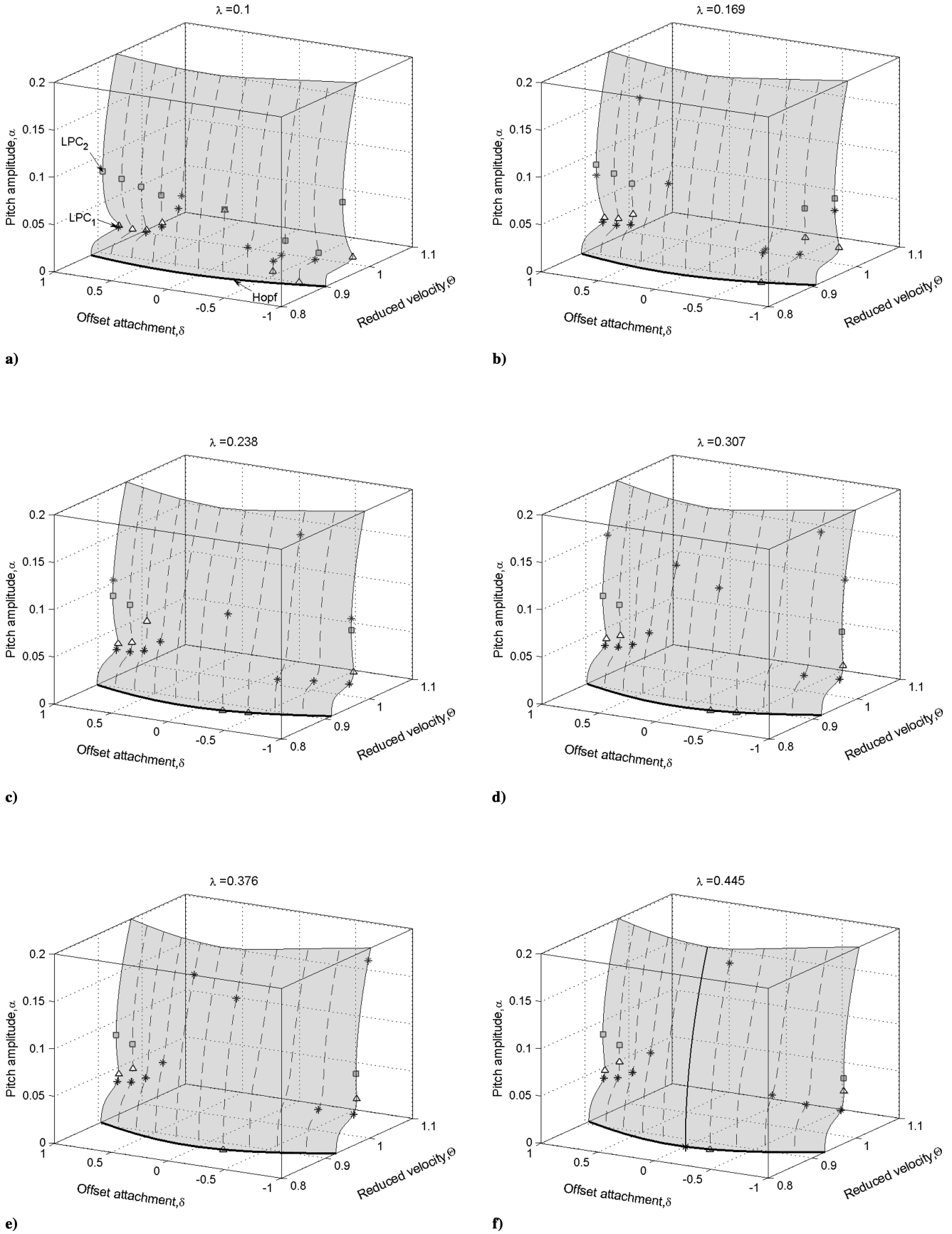

Fig. 13 Surfaces of LCO branches with respect to the damping λ when the series MDOF NES with strong linear coupling is attached to the 2-DOF rigid wing ($\epsilon = 0.02$, $C = 10$). The bold solid line denotes the Hopf bifurcation curve. The triangle (square) indicates the LPC_1 (LPC_2) bifurcation point. The asterisks denote degenerate bifurcation points such as neutral saddle or generalized Hopf.

This is more desirable in practical applications, because less NES mass will provide much better performance in the robustness of instability suppression.

Whereas the Hopf bifurcation surface still exhibits independence of the magnitude of the essential nonlinearity (Fig. 11f), it becomes more dependent on the damping coefficient (Fig. 11e). Referring to the variation of the LCO surfaces with respect to the damping and essential nonlinearity (Figs. 16 and 17, respectively), observe that the LPC bifurcation occurs at the higher reduced velocity or very close to the Hopf point for the positive offsets (i.e., supercritical Hopf or subcritical but with negligible effects on robustness) and at the much lower velocity for the negative offsets (i.e., highly influential subcritical). The subcritical LCOs become more prevalent for higher damping and essential nonlinearity.

C. Robustness Enhancement

From the bifurcation set analysis in Sec. III.B, we can draw a general conclusion. The MDOF NES in series coupling with a strong linear coupling stiffness behaves almost the same as the SDOF NES except for its improved performance in instability suppression. In fact, the MDOF NES with a weak linear coupling stiffness yields an optimization problem. Properly selecting all of the NES parameters such as the overall mass ratio and offset results in an efficient passive vibration controller with a lightweight mass.

In this section, we directly demonstrate enhancing the robustness of instability suppression by comparing the bifurcation behavior of the MDOF NES in series coupling with an SDOF NES with the same NES parameters except for the mass ratio. Time responses will be computed by imposing a strong impulsive perturbation. Furthermore, we analyze the underlying dynamic mechanisms caused by the MDOF NES in terms of instantaneous frequency, and modal energy exchanges and energy dissipation by the NES.

A direct comparison with the bifurcation behavior of the SDOF NES with the same parameter set is examined in a single bifurcation diagram. Figure 18 compares the bifurcation diagrams for the pitch amplitude 1) when no NES is used, 2) when an SDOF NES with mass ratio $\epsilon = 0.02$ and offset $\delta = -1$ is used, and 3) when MDOF NESs with total mass ratios $\epsilon = 0.005, 0.0095, 0.014, 0.0275$ and offsets $\delta = \pm 1$ are used, respectively. All other parameters such as damping, essential nonlinearity, and linear coupling stiffness (weak only in this comparison) are the same for all of the continuation procedures.

The SDOF NES with $\epsilon = 0.02$ (i.e., 2% ratio of the NES mass with respect to the wing mass) and $\delta = -1$ exhibits good performance in suppressing instability in the previous bifurcation analysis (cf. Sec. II). Moreover, its suppression is robust to a degree (up to the reduced velocity $\Theta \approx 0.91$).

The MDOF NES with $\epsilon = 0.005$ (0.5% overall mass ratio) in Fig. 18a provides similar or slightly better suppression behavior; further, this instability suppression is robust up to the reduced velocity $\Theta \approx 0.91$. If the mass of the MDOF NES increases to $\epsilon = 0.095$, slightly below 1% of the wing mass, the robustness enhancement (as denoted by Θ_{RE} in Fig. 18b) becomes pronounced, and robustness is guaranteed up to $\Theta \approx 0.94$ ($\Theta \approx 0.96$) for $\delta = 1$ ($\delta = -1$). Finally, if the mass ratio again increases to $\epsilon = 0.014$ (Fig. 18c), still less than the SDOF NES mass ratio of 2%, the robustness enhancement becomes optimal so that the robustness of instability suppression is guaranteed up to $\Theta \approx 1.0$ ($\Theta \approx 1.01$) for $\delta = 1$ ($\delta = -1$). We note that these reduced velocities are out of the realm of model validity because the amplitudes of uncontrolled aeroelastic responses are beyond the assumption of small motions in the modeling.

Ironically, however, if the total mass ratio of an MDOF NES becomes greater than that of the SDOF NES (Fig. 18d), the robustness of instability suppression by the MDOF NES worsens in comparison with the robustness achieved by the SDOF NES, although it can significantly delay the occurrence of LCOs from the trivial equilibrium position. Recall that there exists an optimal interval of the mass ratio for the series MDOF NES with a weak linear coupling stiffness. Therefore, a well-designed MDOF NES can provide better and more robust suppression behavior than the heavier SDOF NES.

Figure 19 demonstrates enhancing robustness in the time domain by substituting the SDOF NES with 2% mass ratio with the series MDOF NES with 1.4% total mass ratio at the reduced velocity $\Theta = 0.98$. For small initial conditions, the SDOF NES can suppress the instability by the mechanism of recurrent burstouts and suppression (note that the LCO is on the branch between two NS bifurcation points). However, an impulsive disturbance to the heave mode at $\tau = 200$ causes a jump to the LCO branch at the larger amplitude, and the triggering mechanism of instability [6] is recovered (Fig. 19a). On the other hand, the MDOF NES with an even smaller mass ratio retains the suppressed LCOs under the same impulsive disturbance by efficiently transferring the unwanted energy to the NES (Fig. 19b).

Now, we briefly examine the dynamic mechanisms that make robustness enhancement possible with the MDOF NES in series coupling (Lee et al. [1]). First, wavelet transforms (WTs) are performed to examine the instantaneous frequency behavior (i.e., transient resonant interactions between the aeroelastic and NES modes). Then, modal energy exchanges and energy dissipation by the MDOF NES against the input energy are computed.

The instantaneous kinetic and potential energies, which are stored in the masses and springs, respectively, can be written as

$$\begin{aligned}\bar{T}(\tau) &= \tfrac{1}{2}y'(\tau)^2 + x_\alpha y'(\tau)\alpha'(\tau) + \tfrac{1}{2}\alpha'(\tau)^2 + \tfrac{1}{3}\epsilon[v_1'(\tau)^2 \\ &\quad + v_2'(\tau)^2 + v_3'(\tau)^2] \\ \bar{V}(\tau) &= \tfrac{1}{2}\Omega^2 y(\tau)^2 + \tfrac{1}{2}r_\alpha^2\alpha(\tau)^2 + \tfrac{1}{4}\xi_y y(\tau)^4 + \tfrac{1}{4}\xi_\alpha\alpha(\tau)^4 \\ &\quad + \tfrac{1}{4}C[v_1(\tau) - v_2(\tau)]^4 + \tfrac{1}{200}C[v_2(\tau) - v_3(\tau)]^4 \\ &\quad + \tfrac{1}{2}C_1[y(\tau) - \delta\alpha(\tau) - v_1(\tau)]^2\end{aligned} \tag{5}$$

so that the total energy can be computed as

$$E^{\mathrm{total}}(\tau) = \bar{T}(\tau) + \bar{V}(\tau) \tag{6}$$

The energy input from the flow, which is a sum of the energy provided by the initial conditions and the nonconservative work done by the flow, can be expressed by

$$E^{\mathrm{input}}(\tau) = E^{\mathrm{total}}(0) + W_{\mathrm{nc}}^{y}(\tau) + W_{\mathrm{nc}}^{\alpha}(\tau) \tag{7}$$

where

$$W_{\mathrm{nc}}^{y}(\tau) = \mu C_{L,\alpha}\Theta \int_0^\tau \{y'(s) + \Theta\alpha(s)\}y'(s)\,\mathrm{d}s$$

$$W_{\mathrm{nc}}^{\alpha}(\tau) = -\gamma\mu C_{L,\alpha}\Theta \int_0^\tau \{y'(s) + \Theta\alpha(s)\}\alpha'(s)\,\mathrm{d}s$$

The total energy dissipation by the MDOF NES can be written as

$$E_d^{\mathrm{NES}}(\tau) = E_d^{\mathrm{NES1}}(\tau) + E_d^{\mathrm{NES2}}(\tau) \tag{8}$$

where

$$\begin{aligned}E_d^{\mathrm{NES1}}(\tau) &= \epsilon\lambda \int_0^\tau [v_1'(s) - v_2'(s)]^2\,\mathrm{d}s, \\ E_d^{\mathrm{NES2}}(\tau) &= \epsilon\lambda \int_0^\tau [v_2'(s) - v_3'(s)]^2\,\mathrm{d}s\end{aligned} \tag{9}$$

As a result, the instantaneous energy balance is

$$E^{\mathrm{total}}(\tau) = E^{\mathrm{input}}(\tau) - E_d^{\mathrm{NES}}(\tau) \tag{10}$$

We consider the reduced velocity $\Theta = 0.92$ for the study of underlying dynamic mechanisms, for which the complete elimination of instability can be realized with the MDOF NES with $\epsilon = 0.014$, $\lambda = 0.4$, $C = 10$, $C_1 = 0.01$, and $\delta = \pm 1$

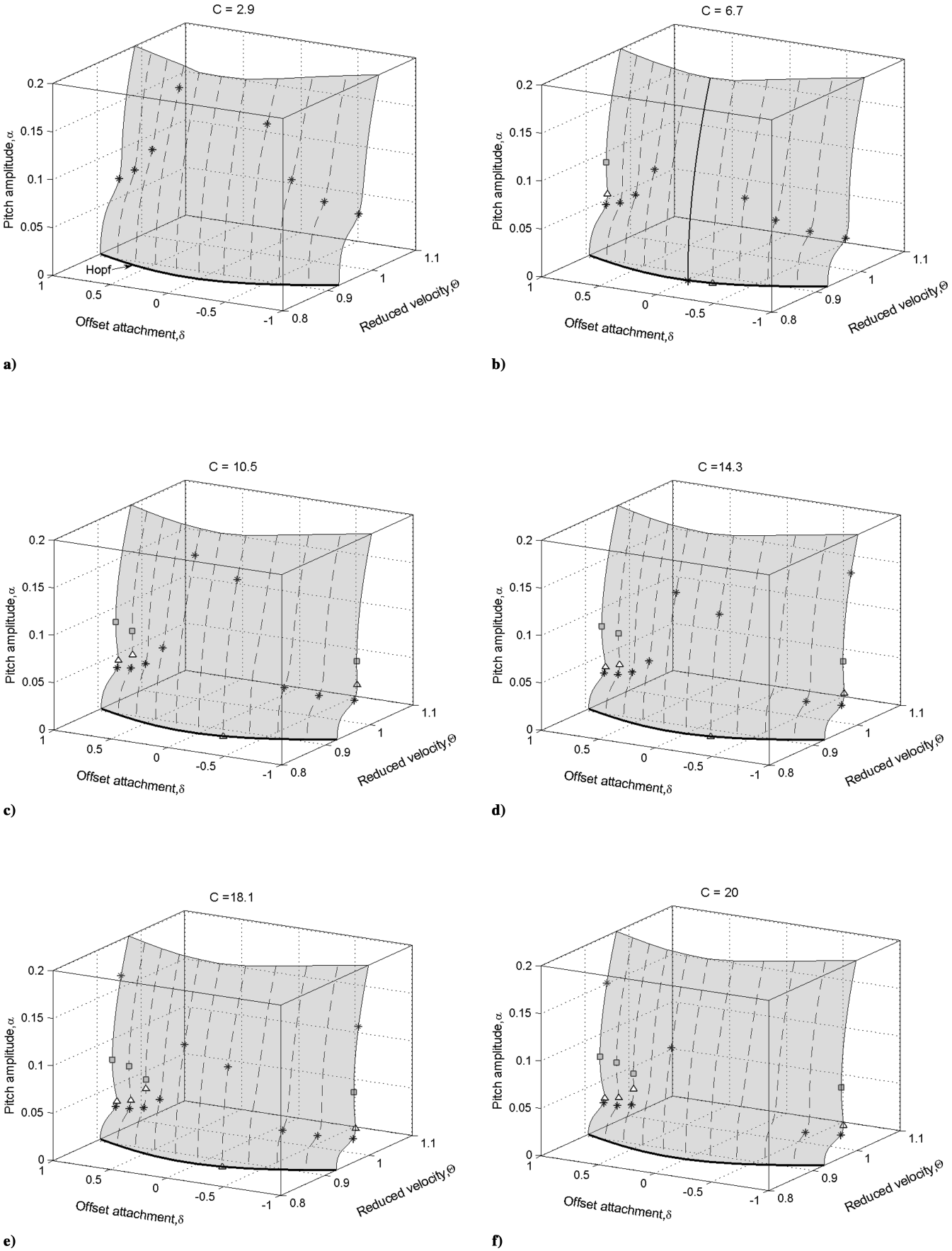

Fig. 14 Surfaces of LCO branches with respect to the essential nonlinearity *C* when the series MDOF NES with strong linear coupling is attached to the 2-DOF rigid wing ($\epsilon = 0.02$, $\lambda = 0.4$). The bold solid line denotes the Hopf bifurcation curve. The triangle (square) indicates the LPC_1 (LPC_2) bifurcation point. The asterisks denote degenerate bifurcation points such as neutral saddle or generalized Hopf.

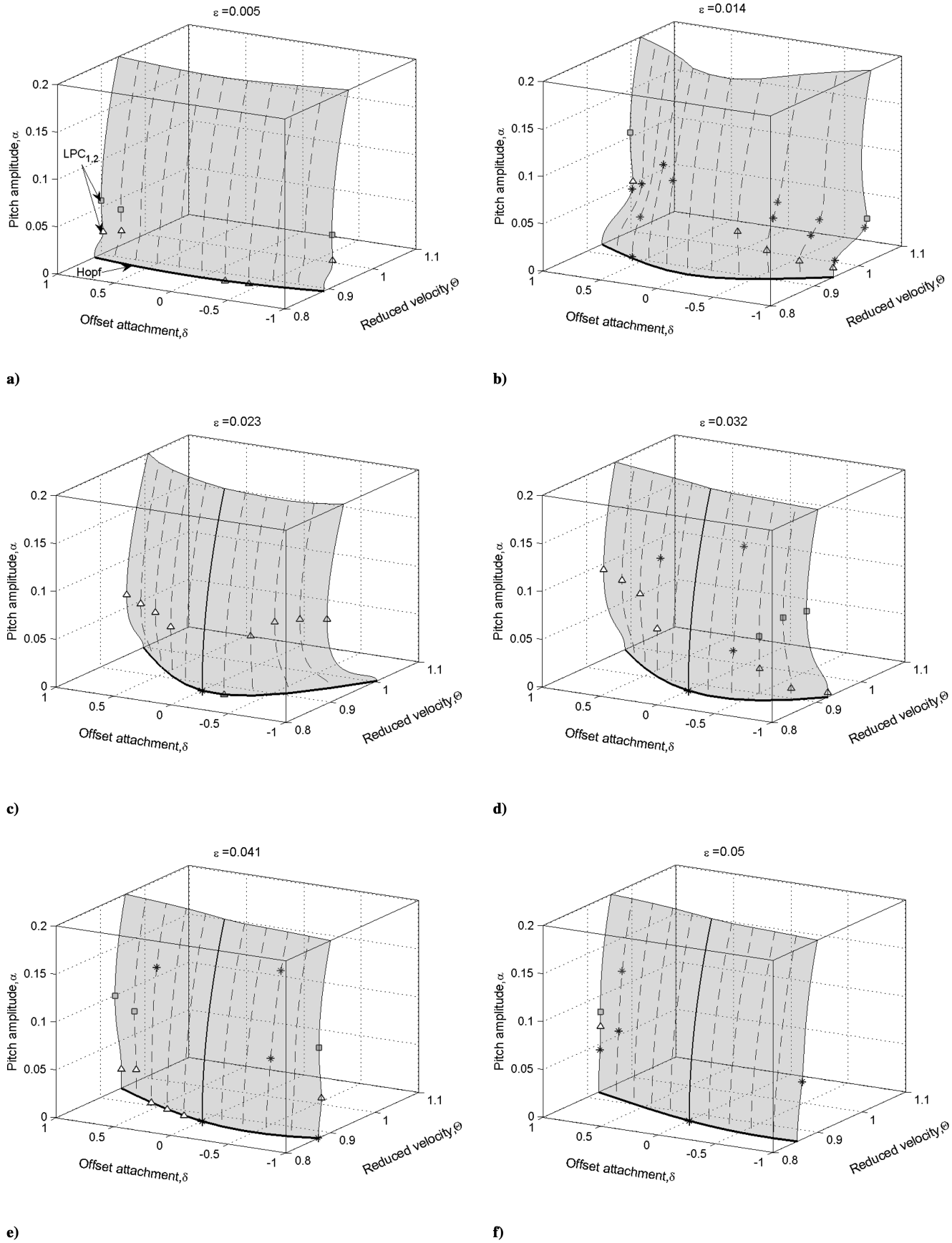

Fig. 15 Surfaces of LCO branches with respect to the mass ratio ϵ when the series MDOF NES with weak linear coupling is attached to the 2-DOF rigid wing ($\lambda = 0.4, C = 10$). The bold solid line denotes the Hopf bifurcation curve. The triangle (square) indicates the LPC_1 (LPC_2) bifurcation point. The asterisks denote degenerate bifurcation points such as neutral saddle or generalized Hopf.

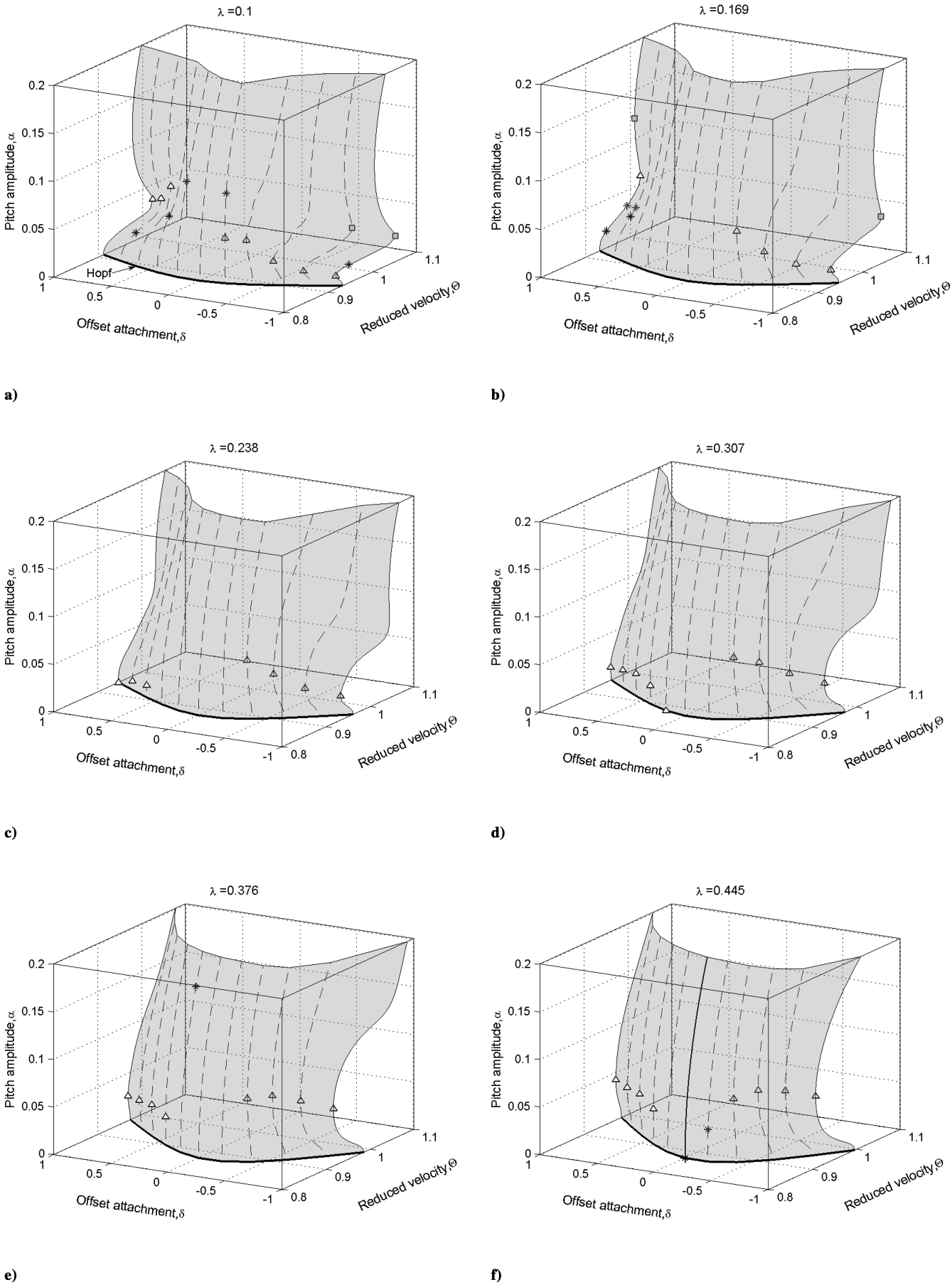

Fig. 16 Surfaces of LCO branches with respect to the damping λ when the series MDOF NES with weak linear coupling is attached to the 2-DOF rigid wing ($\epsilon = 0.02$, $C = 10$). The bold solid line denotes the Hopf bifurcation curve. The triangle (square) indicates the LPC_1 (LPC_2) bifurcation point. The asterisks denote degenerate bifurcation points such as neutral saddle or generalized Hopf.

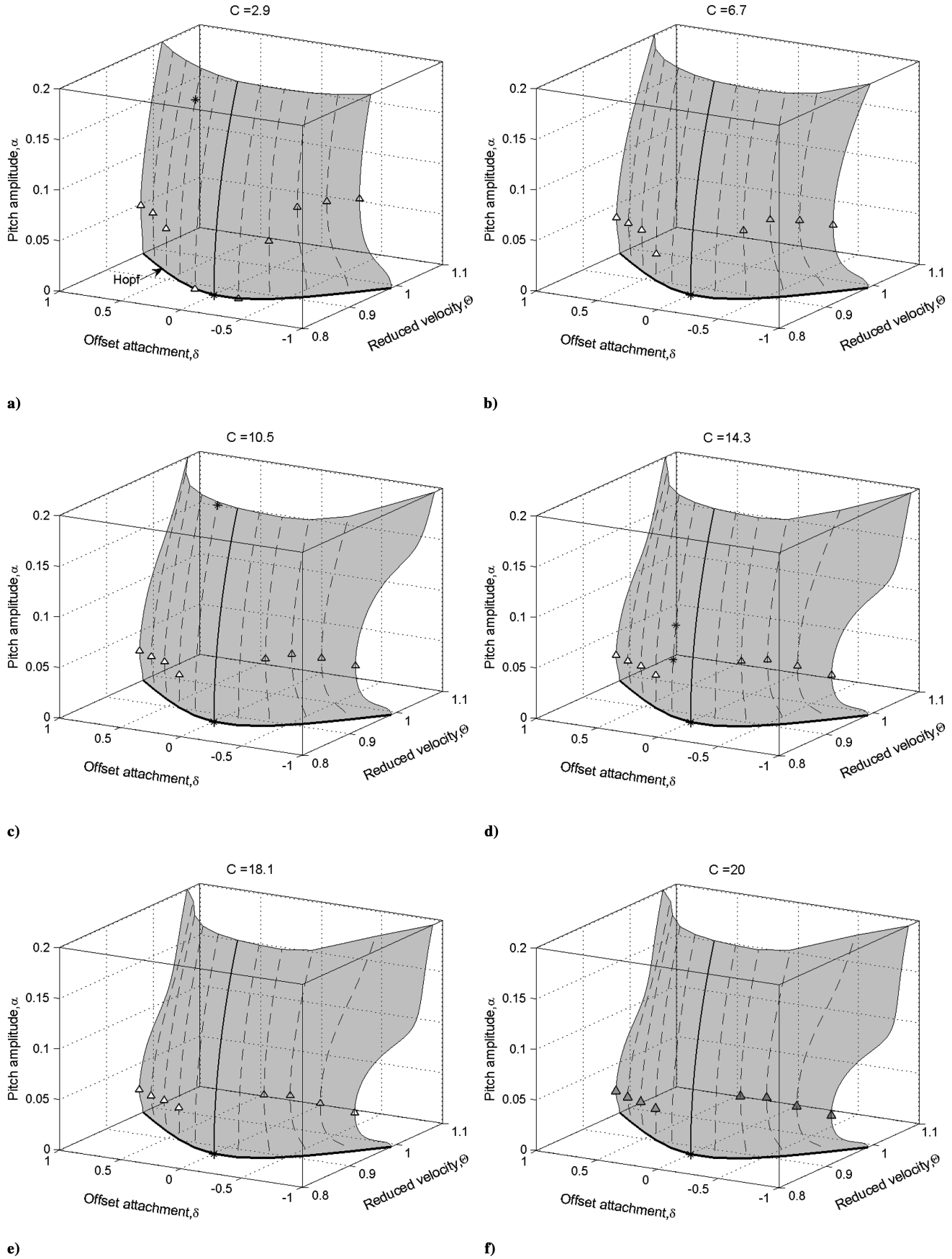

Fig. 17 Surfaces of LCO branches with respect to the essential nonlinearity C when the series MDOF NES with weak linear coupling is attached to the 2-DOF rigid wing ($\epsilon = 0.02, \lambda = 0.4$). The bold solid line denotes the Hopf bifurcation curve. The triangle (square) indicates the LPC_1 (LPC_2) bifurcation point. The asterisks denote degenerate bifurcation points such as neutral saddle or generalized Hopf.

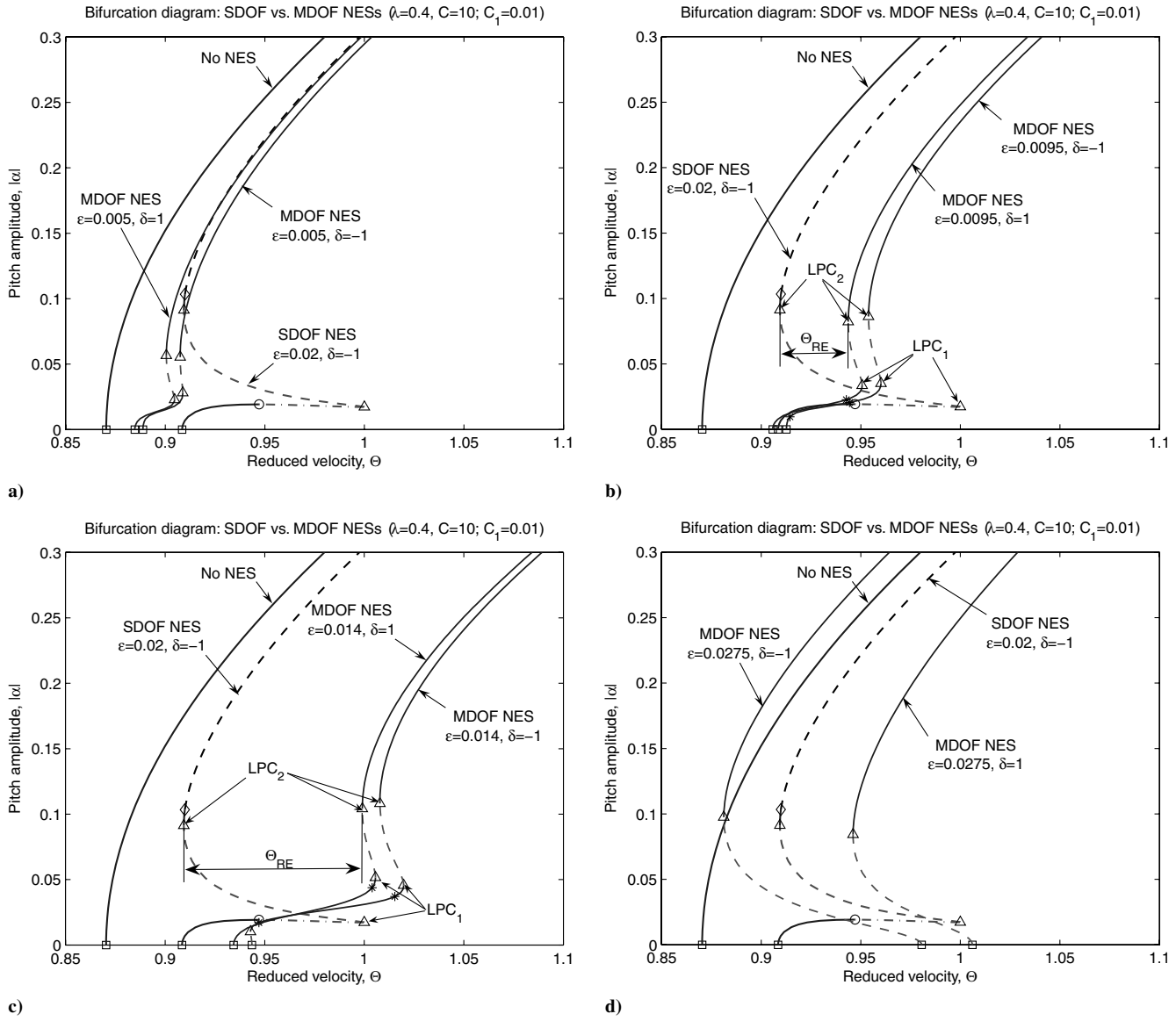

Fig. 18 Comparison of bifurcation diagrams: SDOF vs MDOF NESs. Dashed lines indicate unstable LCO branches. Squares (circles, triangles, diamond, asterisks) indicate the Hopf (Neimark–Sacker, limit point of cycles or saddle node, branch point of cycles, neutral saddle) bifurcation points. Θ_{RE} denotes the amount of the reduced speed for robustness enhancement.

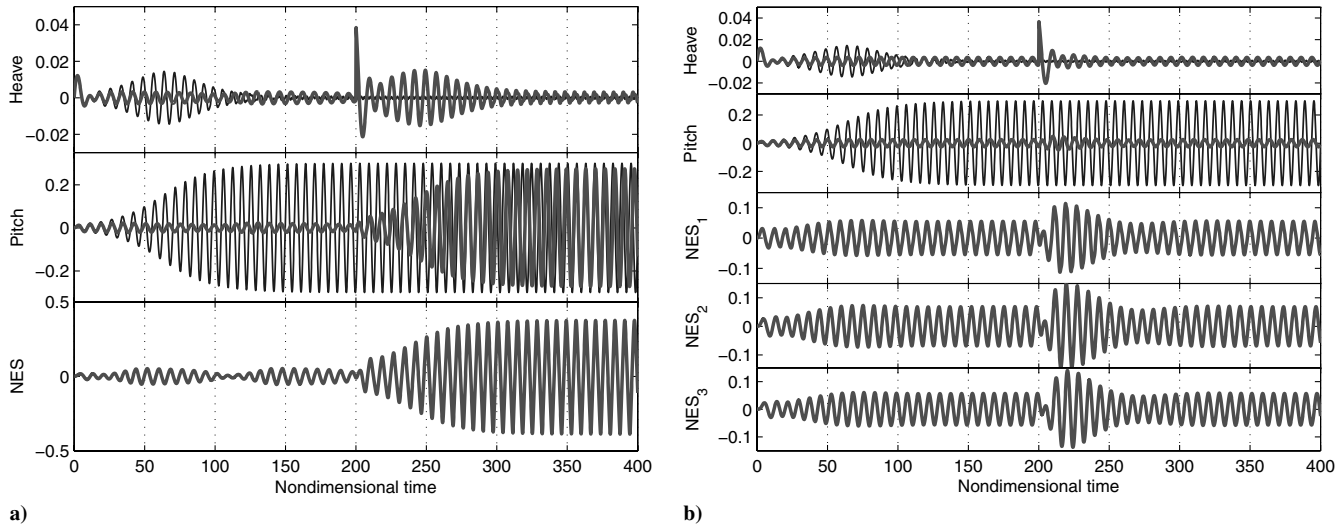

Fig. 19 Demonstration of enhancing robust suppression of instability under the impulsive disturbance of $20 \times y'(0)$ at $\tau = 200$ when $\Theta = 0.98$, $\delta = -1$, $\lambda = 0.4$, $C = 10$, and $C_1 = 0.01$: a) with an SDOF NES ($\epsilon = 0.02$), and b) with an MDOF NES ($\epsilon = 0.014$). The thicker lines indicate the controlled responses.

(cf. Fig. 18c). Zero initial conditions except for the heave velocity are imposed.

Figures 20a and 20b depict time responses when $y'(0) = 0.02$ (a small initial energy input to the heave mode) and $\delta = \pm 1$, respectively, and Figs. 20c and 20d when $y'(0) = 0.1$ (a large initial energy input) and $\delta = \pm 1$. Whether or not the input energy is small, all of the aeroelastic instabilities are completely eliminated by transferring the unwanted energy due to the initial disturbance to the MDOF NES and by dissipating it there. Interestingly, the time to suppress the instability is shorter for the strong impulsive input to the heave mode. In this case, the negative offset initially generates nonlinear beating, through which more vigorous modal energy exchanges are possible.

Instantaneous frequency behavior by means of wavelet transforms of the time responses in Fig. 20 is depicted in Fig. 21. Similar to (but more efficient than) an SDOF NES, a resonant frequency interaction between the heave mode and MDOF NES occurs from 1:1 to subharmonic, and this transient resonant interaction (or capture into resonance [8]) basically plays the role of efficiently prohibiting the initial triggering of the heave mode by the flow before full LCOs are developed (i.e., the full triggering of an instability is completed). The interaction between the pitch mode and the NES is, however, mostly kept captured into 1:1 resonance. The initial nonlinear beat phenomenon for the strong input with a negative offset becomes clearer (Fig. 21d).

Finally, Fig. 22 depicts modal energy exchanges for the time responses in Fig. 20. Because the MDOF NES yields complete elimination of instability, energy balances occur between the input energy and the energy dissipation by the NES so that the total energy remaining in the aeroelastic system becomes exhausted (see the plots in the third row of Fig. 22). The reaction time for this balance becomes shorter for stronger input energy. This observation again proves that more efficient nonlinear energy pumping can be realized for sufficiently large input energy (see, for example, Vakakis and Gendelman [9]).

All cases display the initial strong interaction between the aeroelastic modes and the NES. In other words, the input energy applied to the heave mode is initially absorbed by the NES, with the first mass of the MDOF NES serving as a passage through which unwanted energy in the aeroelastic system flows. Note that the contribution of mass 1 to the total energy is the largest among the three NES masses. This contribution becomes more than 50% for strong input energy. Also, consistent with the previous bifurcation analysis, the weaker linear coupling stiffness provides less resistance for this energy flow.

Then, for small (large) input energy, the next contribution to the total energy goes to the second (third) mass. Furthermore, $E_d^{NES1} > E_d^{NES2}$ for small input energy, but the opposite is true for large input energy. This implies that, for better and more efficient suppression of instabilities by means of an MDOF NES, more energy should be

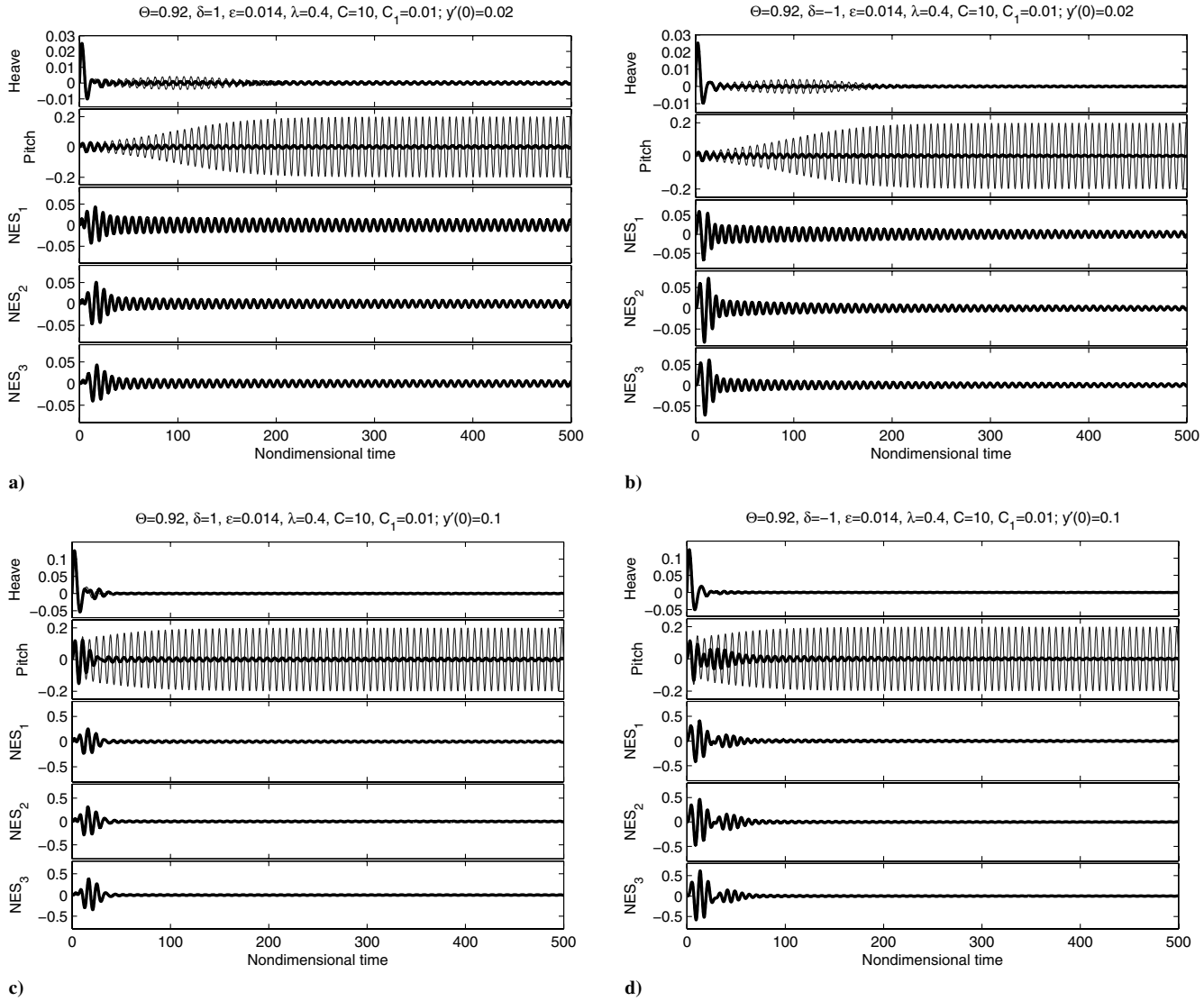

Fig. 20 Wing responses when the MDOF NES is applied for $\Theta = 0.92$, $\epsilon = 0.014$, $\lambda = 0.4$, $C = 10$, and $C_1 = 0.01$. Here, $NES_{1,2,3}$ denote the three masses in the MDOF NES, respectively. The thicker lines indicate the controlled responses.

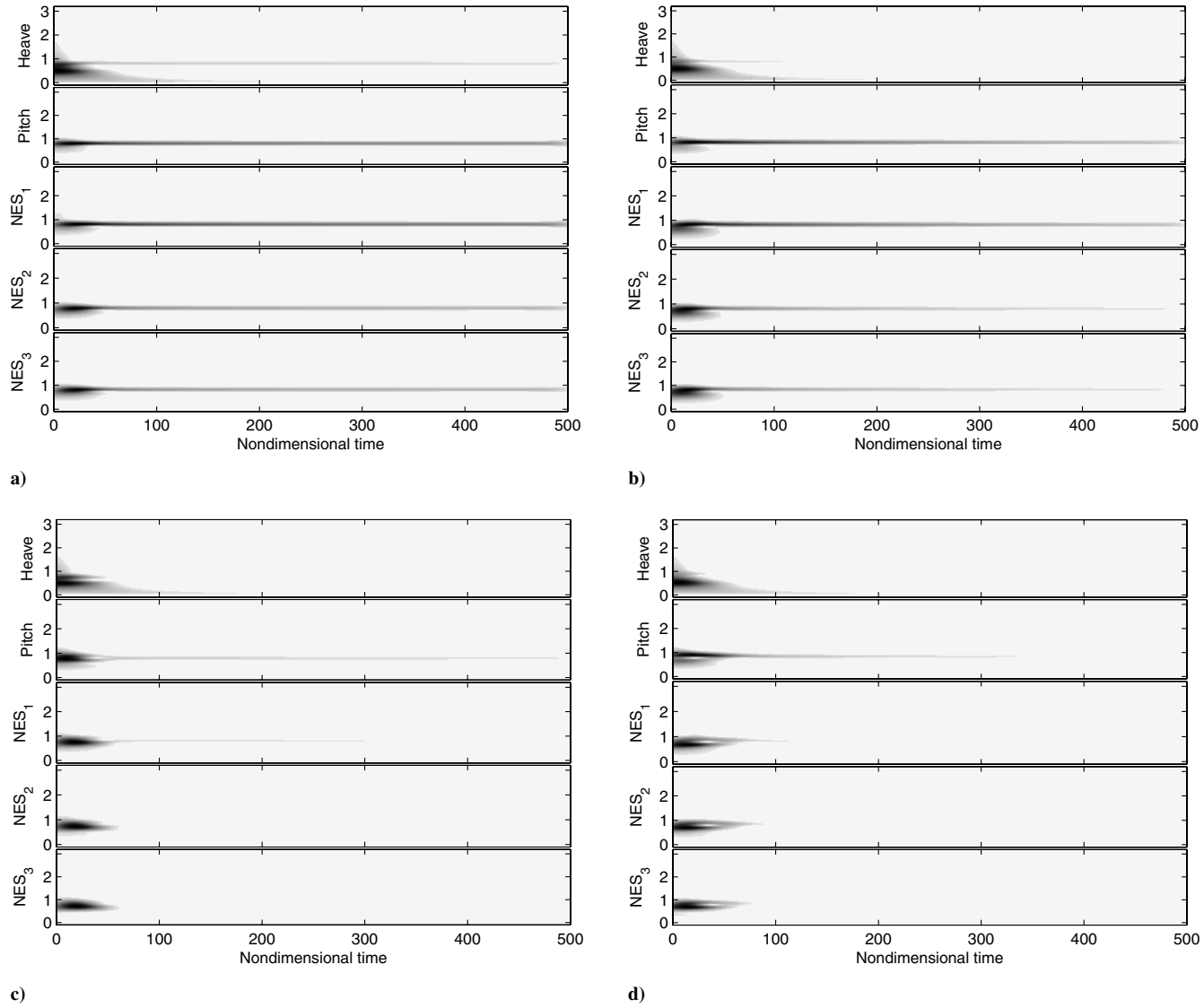

Fig. 21 Wavelet transforms of the responses in Fig. 20.

transferred to the nonlinear attachment furthest from the primary system.

IV. Other Types of MDOF NES Configurations

This section numerically investigates other types of MDOF NES configurations to examine robustness enhancement properties compared with the SDOF NES and MDOF NES in series coupling. Figure 23a is simply the MDOF NES in parallel coupling to the 2-DOF rigid wing; Fig. 23b is the continuous extension of the parallel-coupled MDOF NES but with only 2-DOF itself.

As for a comparable study of the linear vibration absorber, 2-DOF and MDOF tuned mass dampers (TMDs) were studied in Zuo and Nayfeh [10,11], *but to suppress only the single-mode vibration of a primary system*, developing optimization techniques to minimize the response to random and harmonic excitations. They showed that the 2-DOF TMD exhibits better performance than an optimal SDOF linear absorber or two separate absorbers of optimized mass distribution. As already mentioned, the "nonlinear" vibration absorber (i.e., NES) we have considered is totally distinct from the linear one; in particular, if the NES possesses MDOF, it interacts simultaneously with multiple modes of the primary system.

After deriving equations of motion for the systems in Fig. 23, we computed the steady-state pitch amplitude ratios to examine if the action of the parallel-type MDOF NES can yield broadband targeted energy transfers and thus a better (more robust) suppression of instability. Figure 24 presents the results for the parallel MDOF NES with two equal masses close to each edge of the wing. Again, the overall NES mass ratio is chosen to be the same as the that of the SDOF NES.

Unfortunately, the parallel application of the SDOF NESs (and its continuous model, as well) does not yield impressive suppression, compared with the MDOF NES in series coupling (Fig. 10) and even to the SDOF NES of the same overall parameters (Fig. 2). It is obvious that the lumped mass effect of the NES is critical, by recalling the bifurcation analysis in the previous sections in which the mass ratio of the NES (both SDOF and MDOF), together with its offset, are the most influential parameters that affect the efficient and robust suppression of instability.

Therefore, it can be tentatively concluded that multiple SDOF NESs in parallel (or in similar configurations) are not desirable for suppressing aeroelastic instabilities, as long as the mass ratio of the NES to the wing is important. Further studies such as parametric dependence by means of a bifurcation analysis will be required for completeness.

V. Conclusions

To improve the robustness of aeroelastic instability suppression in a rigid wing with structural nonlinearities, we considered several MDOF NES configurations. From the bifurcation analysis of the dynamics of the integrated wing–NES system by means of a

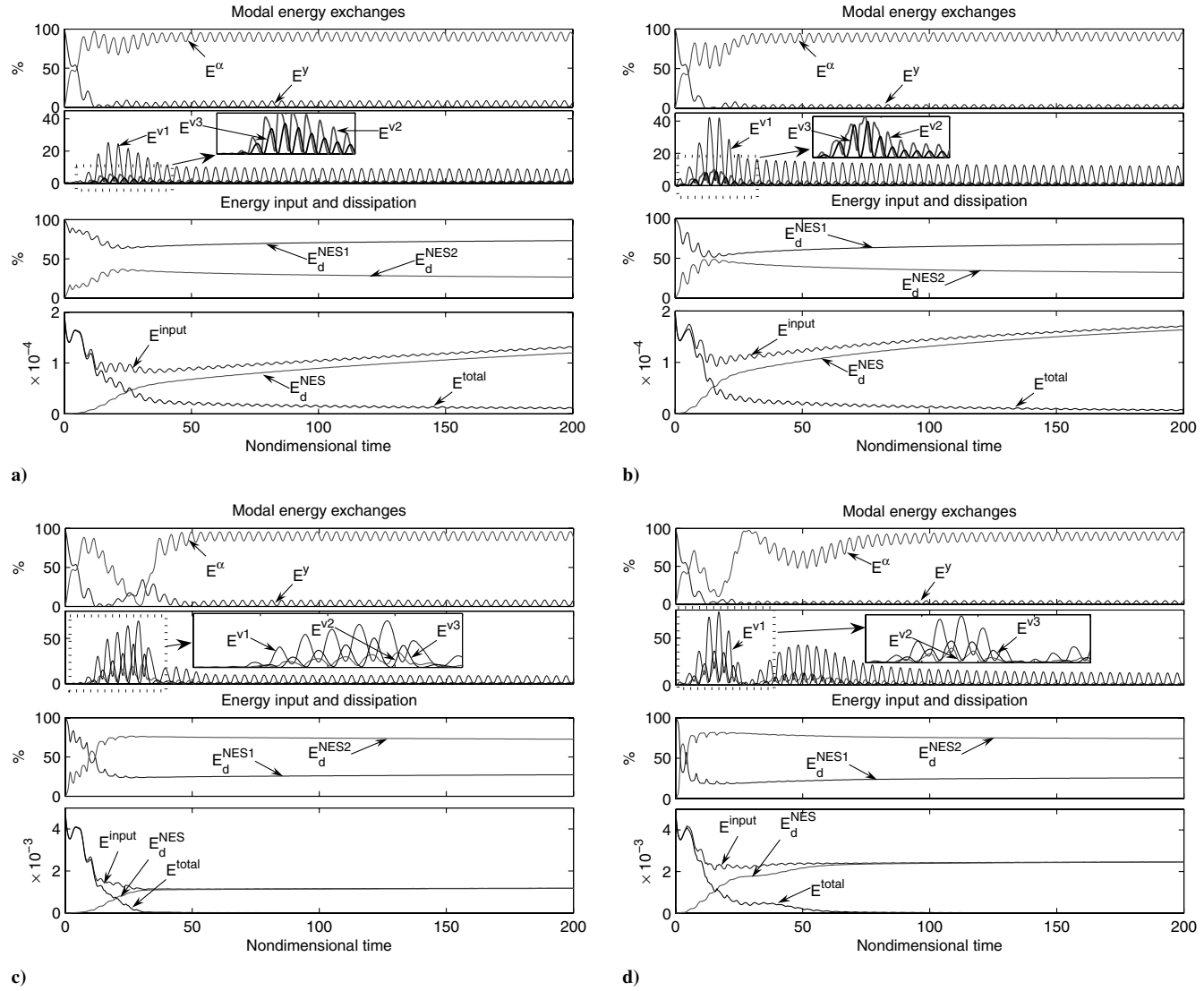

Fig. 22 Nonlinear modal energy exchanges of the responses in Fig. 20.

numerical continuation technique, we showed that the control of the occurrence of the lower LPC bifurcation point above a Hopf bifurcation point is crucial to enhancing robustness. Moreover, we demonstrated that the proposed MDOF NES design (composed of multiple masses coupled in series by means of essentially nonlinear springs and viscous dampers) not only enhances the robustness of LCO suppression against strong impulsive disturbances, but also achieves better or at least comparable suppression performance for smaller total masses compared with SDOF NESs under identical disturbances. Nonlinear modal interactions between the wing and the

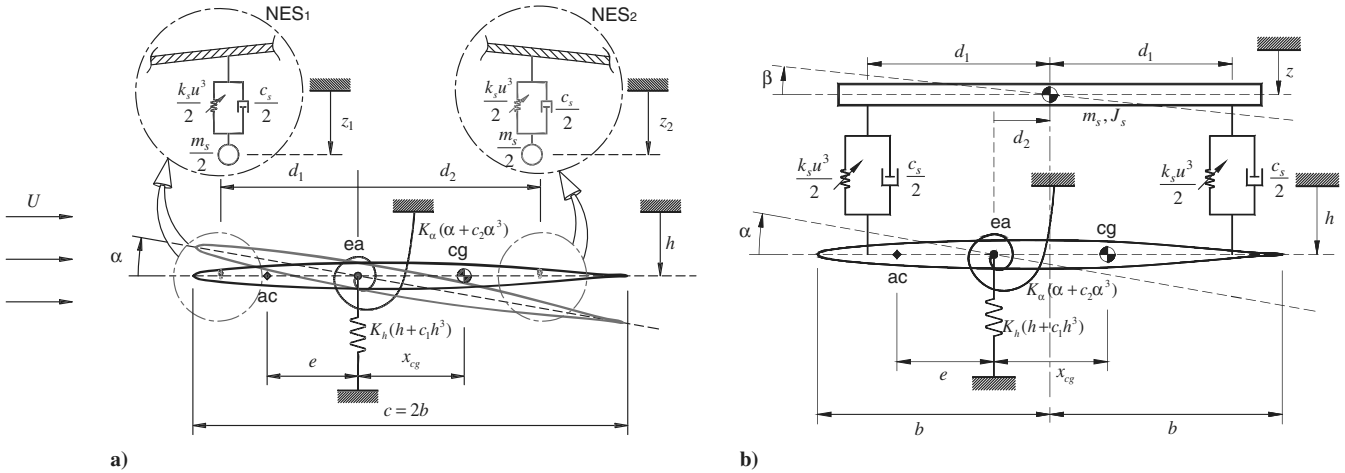

Fig. 23 Application of other types of MDOF NES configurations to the 2-DOF rigid wing: a) MDOF NES in parallel coupling, and b) MDOF NES with a 2-DOF single mass.

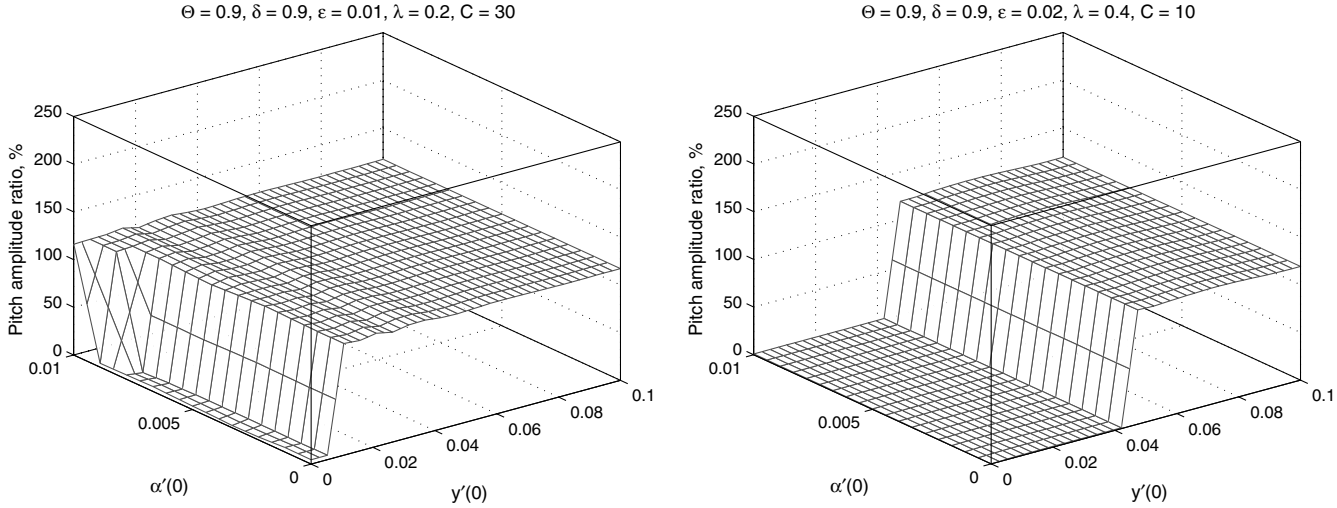

Fig. 24 Dependence of the steady-state pitch amplitude on the initial conditions when the parallel MDOF NES is used ($\delta_1 = \delta_2 = \delta = 0.9$).

attached MDOF NES were studied by means of WTs, as well as the resulting modal energy exchanges. The results suggest that an appropriately designed MDOF NES can greatly improve the robustness of instability suppression. However, an alternative parallel-type MDOF NES did not provide an efficient or robust suppression of LCO instabilities, because of the concentrated mass effect on robustness enhancement. The results reported in this work, which should be viewed in conjunction with previous theoretical and experimental results [1,2], indicate that appropriately designed lightweight passive nonlinear absorbers with essential stiffness nonlinearities can suppress, effectively and robustly, LCO instabilities. As shown in other work [4], the dynamical mechanism governing this suppression is a series of resonance captures that occur between the wing modes and multiple modes of the NES, which results in the broadband passive targeted transfer of unwanted vibration energy from the wing to the NES, where this energy is localized and passively dissipated. However, additional work is needed to study the complex and highly degenerate structure of the dynamics of the integrated structure–MDOF NES system, as well as to determine if unsteady aerodynamic effects significantly alter these results.

Acknowledgment

This work was supported by the U.S. Air Force Office of Scientific Research through grant no. FA9550-04-1-0073. G.K. is supported by a grant from the Belgian National Science Foundation, which is gratefully acknowledged.

References

[1] Lee, Y., Vakakis, A., Bergman, L., McFarland, D. M., and Kerschen, G., "Suppressing Aeroelastic Instability Using Broadband Passive Targeted Energy Transfers, Part 1: Theory," *AIAA Journal*, Vol. 45, No. 3, March 2007, pp. 693–711. doi:10.2514/1.24062

[2] Lee, Y., Kerschen, G., McFarland, D. M., Hill, W., Nichkawde, C., Strganac, T., Bergman, L., and Vakakis, A., "Suppressing Aeroelastic Instability Using Broadband Passive Targeted Energy Transfers, Part 2: Experiments," *AIAA Journal*, Vol. 45, No. 10, Oct. 2007, pp. 2391–2400. doi:10.2514/1.28300

[3] Panagopoulos, P. N., Vakakis, A. F., and Tsakirtzis, S., "Transient Resonant Interactions of Finite Linear Chains with Essentially Nonlinear End Attachments Leading to Passive Energy Pumping," *International Journal of Solids and Structures*, Vol. 41, Nos. 22–23, Nov. 2004, pp. 6505–6528. doi:10.1016/j.ijsolstr.2004.05.005

[4] Tsakirtzis, S., Panagopoulos, P., Kerschen, G., Gendelman, O., Vakakis, A., and Bergman, L., "Complex Dynamics and Targeted Energy Transfer in Linear Oscillators Coupled to Multi-Degree-of-Freedom Essentially Nonlinear Attachments," *Nonlinear Dynamics*, Vol. 48, No. 3, May 2007, pp. 285–318. doi:10.1007/s11071-006-9089-x

[5] Dhooge, A., Govaerts, W., and Kuznetsov, Y., "MATCONT: A Matlab Package for Numerical Bifurcation Analysis of ODEs," *ACM Transactions on Mathematical Software*, Vol. 29, No. 2, 2003, pp. 141–164. doi:10.1145/779359.779362

[6] Lee, Y., Vakakis, A., Bergman, L., McFarland, D. M., and Kerschen, G., "Triggering Mechanisms of Limit Cycle Oscillations in a Two-Degree-of-Freedom Wing Flutter Model," *Journal of Fluids and Structures*, Vol. 21, Nos. 5–7, 2005, pp. 485–529. doi: 10.1016/j.jfluidstructs.2005.08.011

[7] Kuznetsov, Y., *Elements of Applied Bifurcation Theory*, Springer–Verlag, New York, 1995.

[8] Arnold, V., *Dynamical Systems III (Encyclopaedia of Mathematical Sciences)*, Springer–Verlag, Berlin/Heidelberg, Germany, 1988.

[9] Vakakis, A., and Gendelman, O., "Energy Pumping in Coupled Mechanical Oscillators, Part 2: Resonance Capture," *Journal of Applied Mechanics*, Vol. 68, No. 1, Jan. 2001, pp. 42–48. doi:10.1115/1.1345525

[10] Zuo, L., and Nayfeh, S., "Minimax Optimization of Multi-Degree-of-Freedom Tuned-Mass Dampers," *Journal of Sound and Vibration*, Vol. 272, Nos. 3–5, 2004, pp. 893–908. doi:10.1016/S0022-460X(03)00500-5

[11] Zuo, L., and Nayfeh, S., "The Two-Degree-of-Freedom Tuned-Mass Damper for Suppression of Single-Mode Vibration Under Random and Harmonic Excitation," *Journal of Vibration and Acoustics*, Vol. 128, No. 1, Feb. 2006, pp. 56–65. doi:10.1115/1.2128639

C. Cesnik
Associate Editor